Systems genetics analyses in Diversity Outbred mice inform human bone mineral density GWAS and identify *Qsox1* as a novel determinant of bone strength

Basel Al-Barghouthi[1,2,8], Larry D. Mesner[1,6,8], Gina M. Calabrese[1,8], Daniel Brooks[3], Steve M. Tommasini[4], Mary L. Bouxsein[3], Mark C. Horowitz[4], Clifford J. Rosen[5], Kevin Nguyen[1], Samuel Haddox[1], Emily A. Farber[1], Suna Onengut-Gumuscu[1,6], Daniel Pomp[7] and Charles R. Farber[1,2,6]

[1] Center for Public Health Genomics, School of Medicine, University of Virginia, Charlottesville, VA 22908
[2] Department of Biochemistry and Molecular Genetics, School of Medicine, University of Virginia, Charlottesville, VA 22908
[3] Center for Advanced Orthopedic Studies, Beth Israel Deaconess Medical Center, Department of Orthopedic Surgery, Harvard Medical School, Boston, MA 02215
[4] Department of Orthopaedics and Rehabilitation, Yale School of Medicine, New Haven, CT 06520
[5] Maine Medical Center Research Institute, 81 Research Drive, Scarborough, ME 04074
[6] Department of Public Health Sciences, School of Medicine, University of Virginia, Charlottesville, VA 22908
[7] Department of Genetics, University of North Carolina School of Medicine, Chapel Hill, NC 27599
[8] Contributed equally to this work

Correspondence to:

Charles R. Farber
E-mail: crf2s@virginia.edu
Center for Public Health Genomics
University of Virginia
P.O. Box 800717
Charlottesville, VA 22908, USA
Tel. 434-243-8584

ABSTRACT:

Genome-wide association studies (GWASs) for osteoporotic traits have identified over 1000 associations; however, their impact has been limited by the difficulties of causal gene identification and a strict focus on bone mineral density (BMD). Here, we used Diversity Outbred (DO) mice to directly address these limitations by performing the first systems genetics analysis of over 50 complex skeletal phenotypes. We applied a network approach to cortical bone RNA-seq data to discover 46 genes likely to be causal for human BMD GWAS associations, including the novel genes *SERTAD4* and *GLT8D2*. We also performed GWAS in the DO for a wide-range of bone traits and identified *Qsox1* as a novel gene influencing cortical bone accrual and bone strength. Our results provide a new perspective on the genetics of osteoporosis and highlight the ability of the mouse to inform human genetics.

INTRODUCTION:

Osteoporosis is a condition of low bone strength and an increased risk of fracture [1]. It is also one of the most prevalent diseases in the U.S., affecting over 12 million individuals [2]. Over the last decade, efforts to dissect the genetic basis of osteoporosis using genome-wide association studies (GWASs) have been tremendously successful, identifying over 1000 independent associations [3–5]. These data have the potential to revolutionize our understanding of bone biology and discovery of novel therapeutic targets [6,7]; however, progress to date has been limited.

One of the main limitations of human GWAS is the difficulty identifying causal genes. This is largely due to the fact that most associations implicate non-coding variation presumably influencing BMD by altering gene regulation [5]. For other diseases, the use of molecular "-omics" data (*e.g.*, transcriptomic, epigenomic, etc.) in conjunction with systems genetics approaches (*e.g.*, identification of expression quantitative trait loci (eQTL) and network-based approaches) has successfully informed gene discovery [8,9]. However, few "-omics" datasets exist on bone or bone cells in large human cohorts (*e.g*, bone or bone cells were not part of the Gene Tissue Expression (GTEx) project [10]), limiting the use of systems genetics approaches to inform BMD GWAS [11].

A second limitation is that all large-scale GWASs have focused exclusively on bone mineral density (BMD) [3–5]. BMD is a clinically relevant predictor of osteoporotic fracture; however, it explains only part of the variance in bone strength [12–15]. Imaging modalities and bone biopsies can be used to collect data on other bone traits such as trabecular

75 microarchitecture and bone formation rates; however, it will be difficult to apply these
76 techniques “at scale” (N=>100K). Additionally, many aspects of bone, including
77 biomechanical properties, cannot be measured *in vivo*. These limitations have
78 hampered the dissection of the genetics of osteoporosis and highlight the need for
79 resources and approaches that address the challenges faced by human studies.
80
81 The Diversity Outbred (DO) is a highly engineered mouse population derived from eight
82 genetically diverse inbred founders [16]. The DO has been randomly mated for over 30
83 generations and, as a result, it enables high-resolution genetic mapping and relatively
84 efficient identification of causal genes [17,18]. As an outbred stock, the DO also more
85 closely approximates the highly heterozygous genomes of a human population. These
86 attributes, coupled with the ability to perform detailed and in-depth characterization of
87 bone traits and generate molecular data on bone, position the DO as a platform to
88 assist in addressing the limitations of human studies described above.
89
90 Here, we created a resource for the systems genetics of bone strength consisting of
91 information on over 50 bone traits and RNA-seq data from marrow-depleted cortical
92 bone in over 600 DO mice. We demonstrated the utility of this resource in two ways.
93 First, we applied a network approach to the bone transcriptomics data and identified 46
94 bone-associated nodes, whose human homologs are located in BMD GWAS loci and
95 are regulated by colocalizing eQTL. Of the 46, nine were not previously known to
96 influence BMD. Further investigation of two of the nine novel genes, *SERTAD4* and
97 *GLT8D2*, supported them as causal and suggested they influenced BMD via a role in

98 osteoblasts. Second, we performed GWASs for over 50 complex traits associated with
99 bone strength; identifying 28 QTL. By integrating QTL and bone eQTL data, we
100 identified *Qsox1* as the gene responsible for a QTL on Chromosome (Chr.) 1 influencing
101 cortical bone accrual along the medial-lateral femoral axis and femoral strength. These
102 data highlight the power of the DO mouse resource to complement and inform human
103 genetic studies of osteoporosis.

104

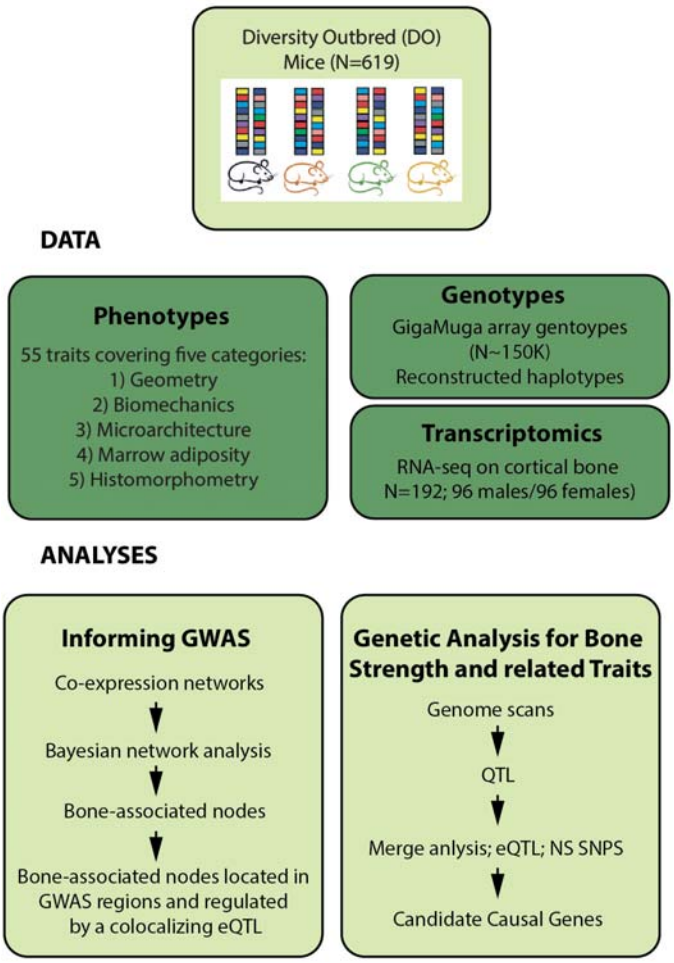

Figure 1. Resource overview. An overview of the resource including data generated and analyses.

RESULTS:

Development of a resource for the systems genetics of bone strength:

An overview of the resource is presented in **Figure 1**. We measured 55 complex skeletal phenotypes in a cohort of DO mice (N=619; 314 males, 305 females; breeding generations 23-33) at 12 weeks of age. We also generated RNA-seq data from marrow-depleted femoral diaphyseal bone (N=192; 96/sex). All mice were genotyped

120 using the GigaMUGA[19] array

121 (~150K SNPs) and these data were used to reconstruct genome-wide haplotype

structures of each mouse. As expected, the genomes of DO mice consisted of approximately 12.5% from each of the eight DO founders (**Supplemental Figure 1A**).

The collection of phenotypes included measures of geometry, microarchitecture, and biomechanics of the femur, along with tibial histomorphometry and marrow adiposity (**Supplemental Table 1)**. Our data included quantification of femoral strength as well as many clinically relevant predictors of strength and fracture risk (*e.g.*, trabecular and cortical microarchitecture). Traits in all categories (except tibial marrow adipose tissue (MAT)) were significantly (P_{adj}<0.05) correlated with femoral strength (**Supplemental Table 2**). Additionally, all traits exhibited substantial variation across the DO cohort. For example, we observed a 30.8-fold variation in trabecular bone volume fraction (BV/TV) of the distal femur and 5.6-fold variation in femoral strength (**Supplemental Figure 1B)**. After adjusting for covariates (age, generation, sex, and body weight) all traits had non-zero heritabilities (h^2) (**Supplemental Figure 1C**). Correlations between traits in the DO were consistent with expected relationships observed in previous mouse and human studies (**Supplemental Table 3)** [20–23].

Identification of bone-associated nodes:

Here, we demonstrate how bone transcriptomic data in the DO can be used to inform human GWAS. First, we partitioned genes into groups based on co-expression by applying Weighted Gene Co-Expression (WGCNA) network analysis to cortical bone RNA-seq data [24]. We generated three WGCNA networks; a sex-combined network as well as sex-specific networks. The three networks contained a total of 124 modules

(**Supplemental Table 4**)**.** A Gene Ontology (GO) analysis revealed that nearly all modules were enriched for genes involved in specific biological processes, including modules enriched for processes specific to bone cells (osteoblasts or osteoclasts) (**Supplemental Table 5**).

We next generated Bayesian networks for each co-expression module, allowing us to model directed gene-gene relationships based on conditional independence. Across the three network sets, we found that genes known to influence bone traits ("known bone gene" list (N=1,539); **Supplemental Table 6**); see methods) were more highly connected than all other genes ($P=2.6 \times 10^{-5}$, $P=5.2 \times 10^{-3}$, and $P=5.5 \times 10^{-7}$ for combined, male, and female network sets, respectively), indicating the structure of the Bayesian networks was not random with respect to connectivity.

To discover genes potentially responsible for GWAS associations, we identified bone-associated nodes (BANs). BANs were defined as genes connected in Bayesian networks with more genes in the "known bone" list than would be expected by chance [25–28]. The analysis identified 1,050 genes with evidence ($P<0.05$) of being a BAN (*i.e.,* sharing network connections with genes known to participate in a bone "regulatory" process) (**Supplemental Table 7**).

Using BANs to inform human BMD GWAS:

We reasoned that the BAN list was enriched for causal BMD GWAS genes. To identify casual BANs, we used data from BMD GWAS and human eQTL data. Of the 1,050 BANs, 900 had human homologs and 544 of those were within 1 Mbp of one of the

1103 BMD GWAS lead SNPs identified in [5]. For each human homolog, we identified local eQTL in non-bone samples using the Gene Tissue Expression (GTEx) project [10,29,30]. We then tested each eQTL for colocalization with their respective BMD GWAS association [3,5]. Of the 544 BANs located in proximity of BMD GWAS loci, 46 had colocalizing eQTL (PPH4>0.75) in at least one GTEx tissue (**Table 1**). Of these, 37 (80.4%) were known regulators of bone biology (based on comparing to the known bone list (N=29) and a literature search for genes influencing bone cell function (N=8)), highlighting the ability of the approach to recover known biology. Based on overlap with the known bone list this represents a highly significant enrichment (OR=7.7, $P=5.5 \times 10^{-14}$). Our approach identified genes such as *SP7* (Osterix) [31], *SOST* [32,33], and *LRP5* [34–36], which play central roles in osteoblast-medicated bone formation. Genes essential to osteoclast activity, such as *TNFSF11* (RANKL) [37–40], *TNFRSF11A* (RANK) [41,42], and *SLC4A2* [43] were also identified. Nine (19.6%) genes were not previously implicated in the regulation of bone traits**.**

One of the advantages of the network approach is the ability to identify potentially causal genes and provide insight into how they impact BMD based on their module membership and network connections. For example, the “cyan” module in the female network (cyan_F) harbored many of the known BANs that influence BMD through a role in osteoclasts (the GO term “osteoclast differentiation” was highly enriched $P=2.8 \times 10^{-15}$ in the cyan_F module) (**Supplemental Table 5**). Two of the nine novel BANs with colocalizing eQTL (**Table 1**), *ATP6V1A* and *PRKCH*, were members of the cyan module in the female network. Based on their cyan module membership it is likely they play a

192 role in osteoclasts. *ATP6V1A* is a subunit of the vacuolar ATPase V1 domain [44]. The
193 vacuolar ATPase plays a central role in the ability of osteoclasts to acidify matrix and
194 resorb bone, though *ATP6V1A* itself has not been directly connected to the regulation of
195 BMD [44]. *PRCKH* encodes the eta isoform of protein kinase C and is highly expressed in
196 osteoclasts [45].
197
198 **Table 1. Homologous human BANs with colocalizing eQTL**

Gene	WGCNA module	PPH4	# neighbors	# bone neighbors	BAN P-value
ADAM12	Brown_F	0.90	13	5	$4.0x10^{-3}$
ARHGAP1	Blue_M	0.99	8	3	$3.2x10^{-2}$
ATP6V1A	Cyan_C	0.87	33	12	$1.5x10^{-5}$
B4GALNT3	Brown_F	0.99	7	3	$1.9x10^{-2}$
BICC1	Brown_C	0.76	16	4	$4.8x10^{-2}$
BMP8A	Yellow_M	0.82	12	5	$3.2x10^{-3}$
CCR1	Cyan_C	0.99	50	11	$4.0x10^{-3}$
CD109	Brown_C	0.82	22	6	$1.1x10^{-2}$
CKB	Cyan_C	0.96	18	9	$8.0x10^{-6}$
DOCK9	Red_F	0.98	9	5	$5.5x10^{-4}$
FAM3C	Brown_C	0.84	30	6	$4.6x10^{-2}$
FAT1	Yellow_M	0.97	8	3	$3.2x10^{-2}$
FGFRL1	Turquoise_F	0.99	11	4	$1.3x10^{-2}$
FRZB	Brown_F	0.99	7	3	$1.9x10^{-2}$
GBA	Cyan_F	0.94	17	5	$1.5x10^{-2}$
GJA1	Brown_C	0.89	11	4	$1.2x10^{-2}$
GLT8D2	Royalblue_M	0.88	21	5	$4.1x10^{-2}$
GREM2	Greenyellow_F	0.99	10	4	$8.9x10^{-3}$
IHH	Red_C	0.89	7	3	$1.9x10^{-2}$
LRP4	Brown_C	0.96	13	4	$2.3x10^{-2}$
LRP5	Yellow_M	0.84	5	3	$7.1x10^{-3}$
MDK	Brown_C	0.97	9	3	$4.0x10^{-2}$
MEPE	Red_F	0.8	20	7	$1.3x10^{-3}$
MMP14	Brown_C	0.83	27	10	$6.3x10^{-5}$
MPRIP	Yellow_M	0.75	15	5	$9.6x10^{-3}$
MRC2	Brown_F	0.99	3	2	$2.3x10^{-2}$

NEK6	Yellow_M	0.97	4	2	$4.6x10^{-2}$
NPR2	Turquoise_M	0.86	8	3	$3.2x10^{-2}$
PKD1	Midnightblue_M	0.86	13	4	$2.7x10^{-2}$
PKDCC	Turquoise_C	0.93	15	4	$3.9x10^{-2}$
PRKCH	Cyan_C	0.78	33	9	$1.9x10^{-3}$
PSTPIP1	Yellow_C	0.88	41	8	$2.6x10^{-2}$
RASD1	Tan_C	0.88	38	8	$1.7x10^{-2}$
SERTAD4	Royalblue_M	0.77	13	6	$6.4x10^{-4}$
SH3RF3	Greenyellow_F	0.99	15	4	$4.0x10^{-2}$
SLC4A2	Cyan_F	0.98	19	7	$9.2x10^{-4}$
SLC7A7	Green_M	0.86	3	2	$2.5x10^{-2}$
SMAD9	Red_C	0.92	22	7	$2.3x10^{-3}$
SOCS2	Brown_F	0.94	6	3	$1.2x10^{-2}$
SOST	Red_C	0.95	24	8	$7.8x10^{-4}$
SP7	Brown_C	0.99	13	4	$2.3x10^{-2}$
SPP1	Cyan_C	0.99	29	7	$1.2x10^{-2}$
THBS3	Darkorange_C	0.98	22	5	$4.1x10^{-2}$
TNFRSF11A	Cyan_F	0.76	9	3	$7.9x10^{-6}$
TNFSF11	Lightcyan_F	0.76	9	4	$5.8x10^{-3}$
UBE2R2	Red_M	0.93	15	4	$4.5x10^{-2}$

Next, we focused on two of the novel BANs with colocalizing eQTL, *SERTAD4* (GTEx Subcutaneous Adipose; coloc PPH4=0.77; PPH4/PPH3=7.9) and *GLT8D2* (GTEx Pituitary; coloc PPH4=0.87; PPH4/PPH3=13.4). Both genes were members of the royalblue module in the male network (royalblue_M). The function of *SERTAD4* (SERTA domain-containing protein 4) is unclear, though proteins with SERTA domains have been linked to cell cycle progression and chromatin remodeling [46]. *GLT8D2* (glycosyltransferase 8 domain containing 2) is a glycosyltransferase linked to nonalcoholic fatty liver disease [47]. The eigengene of royalblue_M module was significantly correlated with several traits, including trabecular number (Tb.N; rho=-0.26; $P=9.5 \times 10^{-3}$) and separation (Tb.Sp; rho=0.27; $P=7.1 \times 10^{-3}$), among others

(**Supplemental Table 8**). The royalblue_M module was enriched for genes involved in processes relevant to osteoblasts such as “extracellular matrix” ($P=8.4 \times 10^{-19}$), “endochondral bone growth” ($P=5.7 \times 10^{-4}$), “ossification” ($P=8.9 \times 10^{-4}$) and “negative regulation of osteoblast regulation” (P=0.04) (**Supplementary Table 5**). Additionally, *Sertad4* and *Glt8d2* were connected, in their local (3-step) Bayesian networks, to well-known regulators of osteoblast/osteocyte biology (such as *Wnt16* [48], *Postn* [49,50], and *Col12a1* [51] for *Sertad4* and *Pappa2* [52], *Pax1* [52,53], and *Tnn* [54] for *Glt8d2*) (**Figure 2A and 2B**). *Sertad4* and *Glt8d2* were strongly expressed in calvarial osteoblasts with expression increasing ($P<2.2 \times 10^{-16}$ and $P=6.4 \times 10^{-10}$, respectively) throughout the course of differentiation (**Figure 2C**). To further investigate their expression in osteoblasts, we generated single-cell RNA-seq (scRNA-seq) data on mouse bone marrow-derived stromal cells. Clusters of cell-types were grouped into mesenchymal progenitors, preadipocytes/adipocytes, osteoblasts, osteocytes, and non-osteogenic cells based on the expression of genes defining each cell-type. *Sertad4* was expressed across multiple cell-types, with its highest expression in a specific cluster (cluster 9) of mesenchymal progenitor cells and lower levels of expression in osteocytes (cluster 10) (**Figure 2D**). *Glt8d2* was expressed in a relatively small number of cells in both progenitor and mature osteoblast populations (**Figure 2D**).

228 Finally, we analyzed data from the International Mouse Phenotyping Consortium (IMPC)

229 for *Glt8d2* [55]. After controlling for body weight, there was a significant ($P=1.5 \times 10^{-3}$)

230 increase in BMD in male *Glt8d2*$^{-/-}$ and no effect (P=0.88) in female *Glt8d2*$^{-/-}$ mice (sex

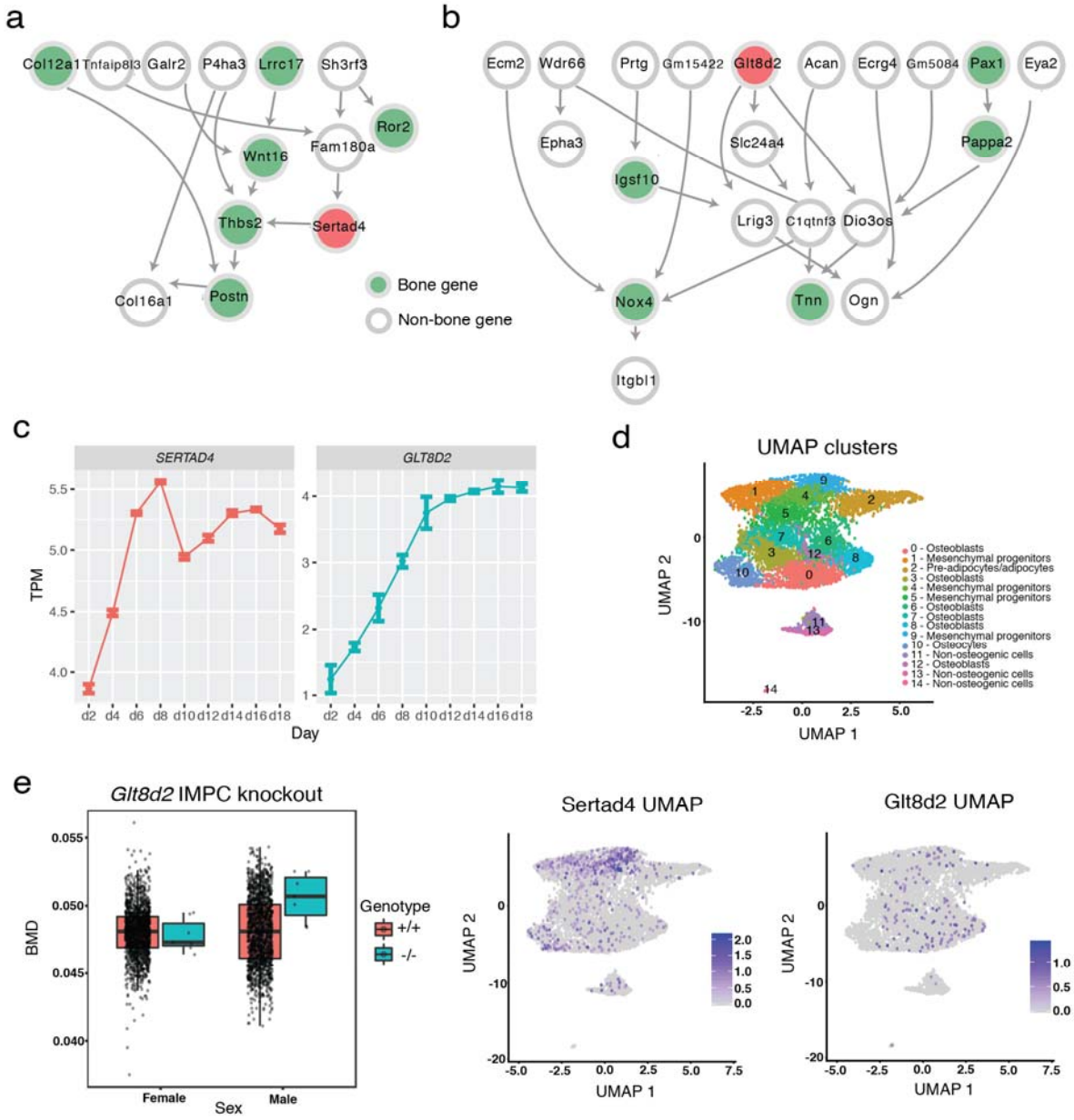

Figure 2. Identifying *SERTAD4* and *GLT8D2* as putative regulators of BMD. a) Local 3-step neighborhood around *Sertad4*. Known bone genes highlighted in green. *Sertad4* highlighted in red. **b**) Local 3-step neighborhood around *Glt8d2*. Known bone genes highlighted in green. *Glt8d2* highlighted in red. **c**) Expression of *Sertad4* and *Glt8d2* in calvarial osteoblasts. **d**) Single cell RNA-seq expression data. Each point represents a cell. The top panel shows UMAP clusters and their corresponding cell-type. The bottom two panels show the expression of *Sertad4* and *Glt8d2.* **e**) Bone mineral density in *Glt8d2* knockout mice from the IMPC.

interaction P= 6.9 x 10^{-3}) **(Figure 2E)**. These data were consistent with the effect direction predicted by the human *GLT8D2* eQTL and eBMD GWAS data where the effect allele of the lead eBMD SNP (rs2722176) was associated with increased *GLT8D2* expression and decreased BMD. Together, these data suggest that *SERTAD4* and *GLT8D2* are causal for their respective BMD GWAS associations and they likely impact BMD through a role in modulating osteoblast-centric processes.

Identification of QTLs for strength-related traits in the DO:

The other key limitation of human genetic studies of osteoporosis has been the strict focus on BMD, though many other aspects of bone influence its strength. To directly address this limitation using the DO, we performed GWAS for 55 complex skeletal traits. This analysis identified 28 genome-wide significant (permutation-derived P<0.05) QTLs for 20 traits mapping to 10 different loci (defined as QTL with peaks within a 1.5 Mbp interval) (**Table 2 and Supplemental Figure 2**). These data are presented interactively in a web-based tool (https://qtlviewer.uvadcos.io/). Of the 10 loci, four impacted a single trait (*e.g.,* medial-lateral femoral width (ML) QTL on Chr2@145.4Mbp), while the other six had apparent pleiotropic effects on more than one trait (*e.g.*, cortical bone morphology traits, cortical tissue mineral density (TMD), and cortical porosity (Ct.Por) QTL on Chr1@155Mbp). The 95% confidence intervals (CIs) for the 21 autosomal associations ranged from 615 Kbp to 5.4 Mbp with a median of 1.4 Mbp.

253 **Table 2. QTL identified for complex skeletal traits in the DO**

Locus	Trait	LOD	Chr	Position (Mbp)	95% CI	# missense variants	Genes with colocalizing eQTL
1	ML	10	1	155.4	155.1 - 155.7	7	*Ier5, Qsox1*
1	Ma.Ar	12.8	1	155.3	155.1 - 155.7	7	*Ier5, Qsox1*
1	Tt.Ar	11.5	1	155.2	155.1 - 156.2	7	*Ier5, Qsox1*
1	TMD	23.9	1	155.1	154.8 - 155.6	7	*Ier5*
1	Ct.Por	11.4	1	155.4	155.1 - 156.4	7	*Ier5, Qsox1*
1	pMOI	8.8	1	155.1	154.8 - 158.2	7	*Ier5, Qsox1*
1	Imax	8.3	1	155.1	155.1 - 158.2	7	*Ier5, Qsox1*
1	Ct.Ar/Tt.Ar	8.5	1	155.3	154.3 - 155.7	7	*Ier5, Qsox1*
2	ML	7.9	2	145.4	144.1 - 145.6	-	-
3	Ma.Ar	8.8	3	68.1	66.6 - 70	8	*Mfsd1, Il12a, Gm17641, 1110032F04Rik*
4	Ma.Ar	8	4	114.6	113 - 118.4	-	-
4	Tt.Ar	8.2	4	114.6	113.6 - 114.8	-	-
5	Ct.Ar/Tt.Ar	8.1	4	127.7	125.4 - 128.1	-	*Csf3r, Gm12946, Clspn, Ncdn, Gm12941, Zmym6, Gm25600*
6	BMD	7.8	8	103.5	102.7 - 104.4	-	-
7	Dfx	10.7	10	23.7	23.3 - 24.6	-	-
7	DFmax	9.4	10	23.7	21.8 - 25.2	-	*C920009B18Rik*
7	W	13.6	10	24.3	23.5 - 24.6	-	-
7	Wpy	11.9	10	23.8	23.5 - 25.3	-	*Rps12, Slc18b1, Stx7*
7	TMD	14.6	10	23.5	23.1 - 24.6	-	-
8	Fmax	8.8	16	23.3	22.3 - 23.4	-	-
8	Ffx	8.2	16	23.1	22.6 - 23.4	-	-
9	Ct.Ar	13.5	X	59.4	58.4 - 71.2	-	-
9	pMOI	10.4	X	59.4	58.4 - 61.4	-	-
9	Imax	11	X	59.5	58.4 - 69.6	-	-
9	Imin	8.4	X	59.5	57.3 - 61.2	-	*Zic3*
10	TbSp	8.6	X	73.8	72.7 - 77.5	-	*Pls3*
10	Tb.N	7.9	X	74	72.7 - 76.8	-	*Fundc2, Cmc4, Pls3*
10	Ct.Th	9.9	X	73.4	58.4 - 74.1	-	-

254

255

Overlap with human BMD GWAS:

We anticipated the genetic analysis of bone strength traits in DO mice would uncover novel biology not captured by human BMD GWAS. To evaluate this prediction, we identified overlaps between the 10 identified mouse loci and 1103 human BMD GWAS associations [5]. Of the 10 mouse loci, the human syntenic regions (**Supplemental Table 9**) for six (60%) contained at least one independent GWAS association (**Supplemental Figure 3**). We calculated the number expected by chance by randomly selecting 10 human regions (of the same size) 1000 times and identifying overlaps. Six overlaps corresponded to the 56th percentile of the null distribution. While it is impossible at this point to know how many of the identified mouse QTL involve genes that influence BMD, these results are consistent with the idea that some of the QTL in the DO are due to genes involved in processes influencing aspects of bone other than BMD.

Identification of potentially causal genes:

For each locus, we defined the causal gene search space as the widest confidence interval given all QTL start and end positions ±250 Kbp. We then used merge analysis to identify likely causal genes. Merge analyses were performed by imputing all known variants from the genome sequences of the eight founders onto haplotype reconstructions for each DO mouse and then performing single variant association tests. We focused on variants in the top 15% of each merge analysis as those are most likely to be causal [56].

We next identified missense variants that were top merge analysis variants common to all QTL in a locus. We identified seven missense variants in locus 1, and eight missense variants in locus 3 (**Table 2**). Of the seven missense variants in locus 1, three (rs243472661, rs253446415, and rs33686629) were predicted to be deleterious by SIFT. They are all variants in the uncharacterized protein coding gene *BC034090*. In locus 3, three (rs250291032, rs215406048 and rs30914256) were predicted to be deleterious by SIFT (**Supplemental Table 10**). These

282 variants were located in myeloid leukemia factor 1 (*Mlf1*), Iqcj and Schip1 fusion protein
283 (*Iqschfp*), and Retinoic acid receptor responder 1 (*Rarres1*), respectively.
284
285 We next used the cortical bone RNA-seq data to map 10,399 local eQTL (**Supplemental Table**
286 **11**). Of these, 174 local eQTL regulated genes located within bone trait QTL. To identifying
287 colocalizing eQTL, we identified trait QTL/eQTL pairs whose top merge analysis variants
288 overlapped. This analysis identified 18 genes with colocalizing eQTL in 6 QTL loci (**Table 2**).
289
290 **Characterization of a QTL on Chromosome 1 influencing bone geometry:**
291 Locus 1 (Chr1) influenced cortical bone geometry (Ma.Ar, total cross sectional area (Tt.Ar),
292 medial-lateral femoral width (ML), polar moment of inertia (pMOI), cortical bone area fraction
293 (Ct.Ar/Tt.Ar), and maximum moment of inertia (I_{max})), tissue mineral density (TMD), and cortical
294 porosity (Ct.Por) (**Figure 3A**). We focused on this locus due to its pleiotropic nature, strong
295 effect size, and the identification of candidate genes (*Ier5*, *Qsox1,* and *BC034090*) (**Table 2**).
296 Additionally, we had previously measured ML in two independent cohorts of DO mice from
297 earlier generations and a QTL scan of those data uncovered the presence of a similar QTL on
298 Chr1 (**Supplemental Figure 4**). The identification of this locus across two different DO cohorts
299 (which differed in generations, diets, and ages) provided robust replication justifying further
300 analysis.
301
302 We next tested if the locus pleiotropically affected all traits or if it was due to multiple linked
303 QTL. We primarily tested the hypothesis that the genetic effects on bone geometry and TMD
304 were distinct (as one might expect). The non-reference alleles of the top merge analysis
305 variants for each QTL were private to WSB/EiJ. To test if these variants explained all QTL, we
306 performed the same association scans for each trait, but included the genotype of the lead ML
307 QTL variant (rs50769082; 155.46 Mbp; ML was used as a proxy for all the cortical morphology

308 traits) as an additive covariate. This led to the ablation of all QTL except for TMD which
309 remained significant (**Figure 3B**). We then repeated the analysis using the lead TMD QTL
310 variant (rs248974780; 155.06 Mbp) as an additive covariate (**Figure 3C**). This led to the
311 ablation of all QTLs. These results supported the presence of at least two loci both driven by

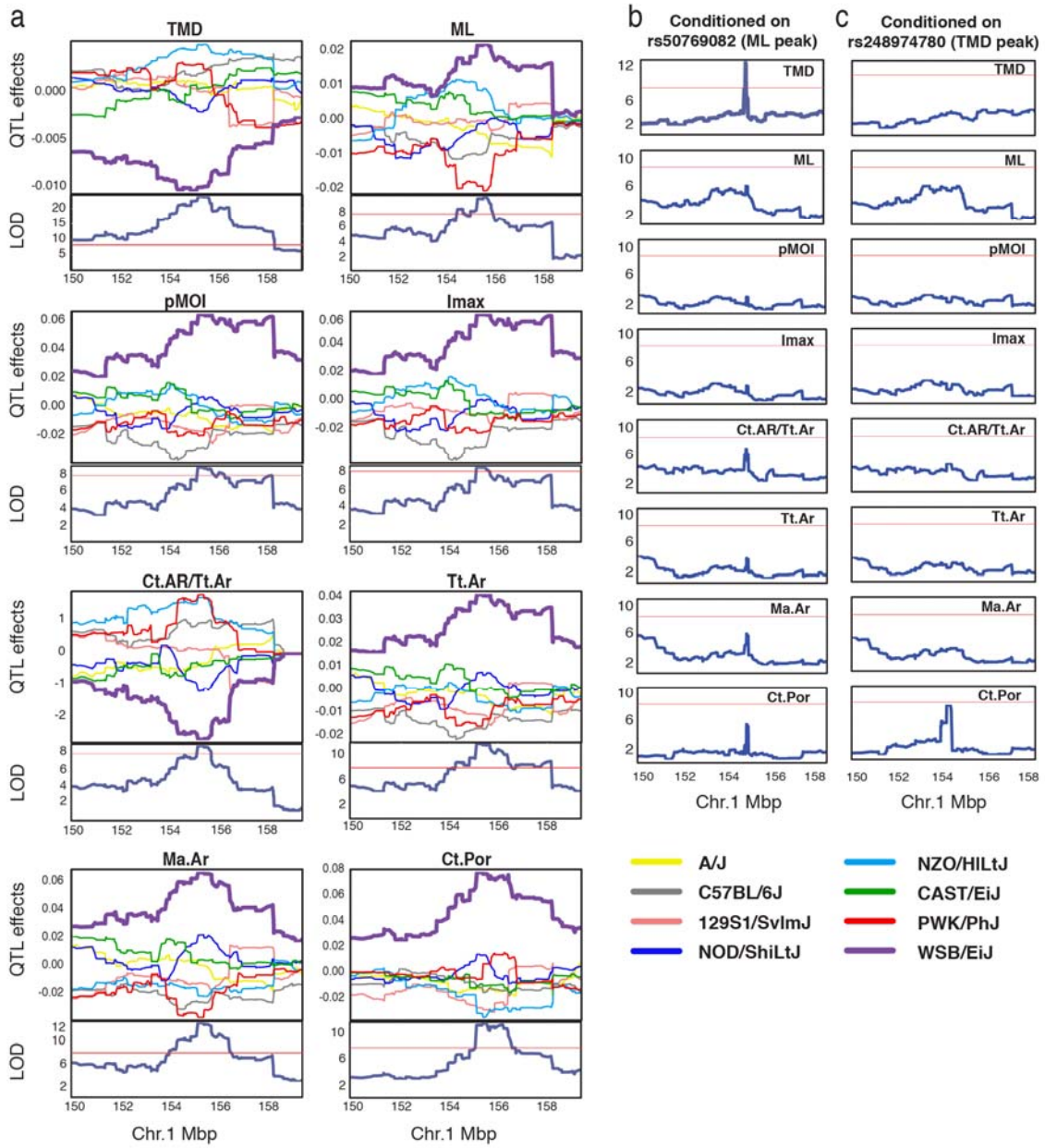

Figure 3. QTL (locus 1) on chromosome 1. a) For each plot, the top panel shows allele effects for the DO founders for each of the 8 QTL across an interval on chromosome 1 (Mbp, colors correspond to the founder allele in the legend). Bottom panels show each respective QTL scan. The red horizontal lines represent LOD score thresholds (Genome-wide P<=0.05). **b**) QTL scans across the same interval as panel (A), after conditioning on rs50769082. **c**) QTL scans after conditioning on rs248974780.

WSB/EiJ alleles, one influencing cortical bone geometry and Ct.Por and the other TMD.

Qsox1 is responsible for the effect of locus 1 on cortical bone geometry:

Given the importance of bone geometry to strength, we sought to focus on identifying the gene(s) underlying locus 1 impacting cortical bone geometry. We re-evaluated candidate genes in light of the evidence for two distinct QTL. Immediate Early Response 5 (*Ier5)* and quiescin sulfhydryl oxidase 1 (*Qsox1*) were identified as candidates based on the eQTL analysis and *BC034090* as a candidate based on nonsynonymous variants (**Table 2**). Interestingly, *Ier5* and *Qsox1* eQTL colocalized with all QTL, except the TMD QTL, where only *Ier5* colocalized (**Table 2 and Figure 4A**). We cannot exclude the involvement of the nonsynonymous variants in *BC034090*; however, without direct evidence that they impacted *BC034090* function, we put more emphasis on the eQTL. As a result, based on its colocalizing eQTL and known biological function (see below), we predicted that *Qsox1* was at least partially responsible for locus 1.

QSOX1 is the only known secreted catalyst of disulfide bond formation and a regulator of extracellular matrix integrity [57]. It has not been previously linked to skeletal development. We found that *Qsox1* was highly expressed in calvarial osteoblasts and its expression decreased ($P=6.4 \times 10^{-6}$) during differentiation (**Figure 4B**). In scRNA-seq on bone marrow-derived stromal cells, we observed *Qsox1* expression in all osteogenic cells with its highest expression seen in a cluster of mesenchymal progenitors defined by genes involved in skeletal development such as *Grem2*, *Lmna*, and *Prrx2* (cluster 1) (**Supplemental Table 12 and Figure 4C**). Additionally, in the DO cortical bone RNA-seq data, *Qsox1* was highly co-expressed with many key regulators of skeletal development and osteoblast activity (*e.g.*, *Runx2*; rho=0.48, $P=<2.2 \times 10^{-16}$, *Lrp5*; rho=0.41, $P=6.2 \times 10^{-9}$).

To directly test the role of *Qsox1*, we used CRISPR/Cas9 to generate *Qsox1* mutant mice. We generated five different mutant lines harboring unique mutations, including two 1-bp frameshifts, a 171-bp in-frame deletion of the QSOX1 catalytic domain, and two large deletions (756 bp and 1347 bp) spanning most of the entire first exon of *Qsox1* (**Figure 5A, Supplemental Tables 13 and 14**). All five mutations abolished QSOX1 activity in serum (**Figure 5B**). Given the uniform lack of QSOX1 activity, we combined phenotypic data from all lines to evaluate the effect of QSOX1 deficiency on bone. We hypothesized based on the genetic and eQTL data, that QSOX1 deficiency would increase all traits mapping to locus 1, except TMD. Consistent with this prediction, ML was increased in male ($P=4.17x10^{-11}$) and female ($P=0.012$) mice as a function of *Qsox1* mutant genotype (**Figure 5C**). Also consistent with the genetic data, we observed no difference in other

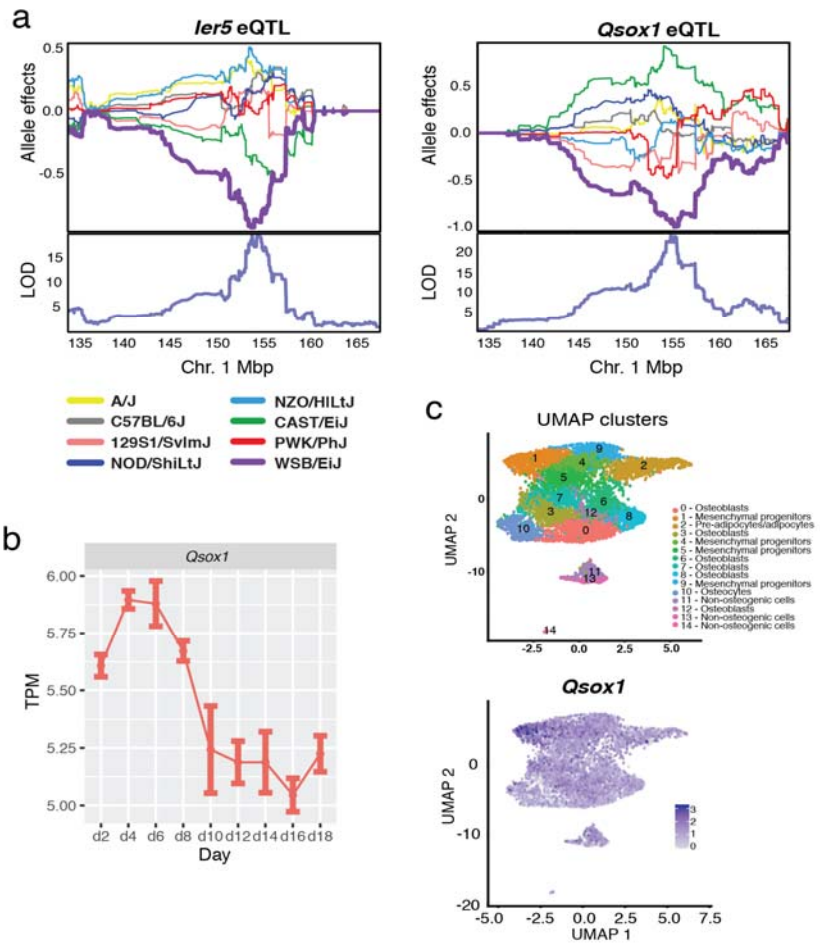

Figure 4. Characterization of *Qsox1*. **a**) The top panel shows allele effects for the DO founders for *Ier5* and *Qsox1* expression an interval on chromosome 1 (Mbp, colors correspond to the founder allele in the legend). Y-axis units are best linear unbiased predictors (BLUPs). Bottom panels show each respective QTL scan. LOD score threshold for autosomal eQTL is 10.89 (alpha=0.05). **b**) *Qsox1* expression in calvarial osteoblasts. **c**) Single cell RNA-seq expression data. Each point represents a cell. The top panel shows UMAP clusters and their corresponding cell-type. The bottom panel shows the expression of *Qsox1.*

gross morphological traits including femoral anterior-posterior femoral width (AP) (P=0.17) and femoral length (FL) (P=0.99). We next focused on male *Qsox1*$^{+/+}$ and *Qsox1*$^{-/-}$ mice and used microCT to measure other bone parameters. We observed increased pMOI (P=0.02) (**Figure 5D**), Imax (P=0.009) (**Figure 5E**), and Ct.Ar/Tt.Ar (P=0.031) (**Figure 5F**). Total area (Tt.Ar) (**Figure 5G**) was increased, but the difference was only suggestive (P=0.08). Marrow area (Ma.Ar, P=0.93) was not different (**Figure 5H**). We observed no change in TMD (P=0.40) (**Figure 5I**). We also observed no difference in cortical porosity (Ct.Por) (P=0.24) (**Figure 5J**).

Given the strength of locus 1 on bone geometry and its association with biomechanical strength, we were surprised the locus did not impact femoral strength. Typically, in four-point bending assays, the force is applied along the AP axis. We replicated this in

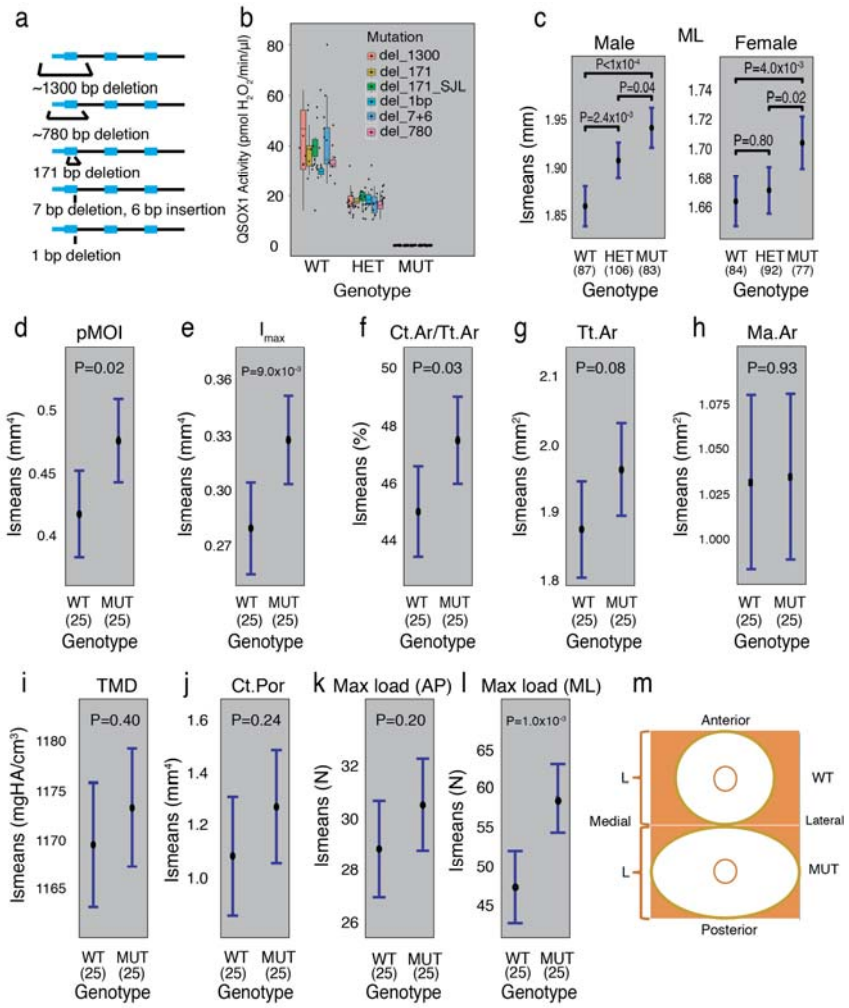

Figure 5. *Qsox1* is responsible for several chromosome 1 QTL. a) Representative image of the *Qsox1* knockout mutations. **b**) QSOX1 activity assay in serum. Data is grouped by mouse genotype. **c**) Caliper-based measurement of femoral medial-lateral width in *Qsox1* knockout mice. **d-j**) microCT measurements of chromosome 1 QTL phenotypes in *Qsox1* knockout mice. **k**) Bone strength (max load, F_{max}) in the AP orientation, measured via four-point bending. **l**) Bone strength (max load, F_{max}) in the ML orientation, measured via four-point bending. **m**) Cross-sectional model of the effect of *Qsox1* on bone size. In this model, W represents equal AP widths.

386 femurs from *Qsox1*$^{+/+}$ and *Qsox1*$^{-/-}$ mice and saw no significant impact on strength (P=0.20)
387 (**Figure 5K**). However, when we tested femurs by applying the force along the ML axis, we
388 observed a significant increase in strength in *Qsox1*$^{-/-}$ femurs (P=1.0 x 10^{-3}) (**Figure 5L**).
389 Overall, these data demonstrate that absence of QSOX1 activity leads to increased cortical
390 bone accrual specifically along the ML axis (**Figure 5M**).
391

392 **Discussion:**

393 Human GWASs for BMD have identified over 1000 loci. However, progress in causal
394 gene discovery has been slow and BMD explains only part of the variance in bone
395 strength and the risk of fracture [7]. The goal of this study was to demonstrate that
396 systems genetics in DO mice can help address these limitations. Towards this goal, we
397 used cortical bone RNA-seq data in the DO and a network-based approach to identify
398 46 genes likely causal for BMD GWAS loci. Nine of the 46 were novel. We provide
399 further evidence supporting the causality of two of these genes, *SERTAD4* and
400 *GLT8D2*. Furthermore, GWAS in the DO identified 28 QTLs for a wide-range of strength
401 associated traits. From these data, *Qsox1* was identified as a novel genetic determinant
402 of cortical bone mass and strength. These data highlight the power of systems genetics
403 in the DO and demonstrate the utility of mouse genetics to inform human GWAS and
404 bone biology.
405

406 To inform BMD GWAS, we generated Bayesian networks for cortical bone and used
407 them to identify BANs. Our analysis was similar to “key driver” analyses [25–27] where the
408 focus has often been on identifying genes with strong evidence (P_{adj}<0.05) of playing
409 central roles in networks. In contrast, we used BAN analysis as a way to rank genes

based on the likelihood that they are involved in a biological process important to bone (based on network connections to genes known to play a role in bone biology). We then honed in on those genes most likely to be responsible for BMD GWAS associations by identifying BANs regulated by human eQTL that colocalize with BMD GWAS loci. Together, a gene being both a BAN in a GWAS locus and having a colocalizing eQTL is strong support of causality. This is supported by the observation that 80% of the 46 BANs with colocalizing eQTL were bona fide regulators of BMD.

One advantage of our network approach was the ability to not only identify causal genes, but also to use network information to predict the cell-type through which these genes are likely acting. We demonstrate this idea by investigating the two novel BANs with colocalizing eQTL from the royalblue_M module. The royalblue_M module was enriched in genes involved in bone formation and ossification, suggesting that the module as a whole and its individual members were involved in osteoblast-driven processes. This prediction was supported by the role of genes in osteoblasts that were directly connected to *Sertad4* and *Glt8d2*, the expression of the two genes in osteoblasts, and for *Glt8d2*, its regulation of BMD *in vivo*. Little is known regarding the specific biological processes that are likely impacted by *Sertad4* and *Glt8d2* in osteoblasts; however, it will be possible to utilize this information in future experiments designed to investigate their specific molecular functions. For example, *Sertad4* was connected to *Wnt16*, *Ror2*, and *Postn* all of which play roles in various aspects of osteoblast/osteocyte function. Wnt signaling is a major driver of osteoblast-mediated bone formation and skeletal development [58]. Interestingly, *Wnt16* and *Ror2* play central

433 roles in canonical (*Wnt16*) and non-canonical (*Ror2* in the *Wnt5a*/*Ror2* pathway) Wnt
434 signaling [59] and have been shown to physically interact in chondrocytes [60]. *Postn* has
435 also been shown to influence Wnt signaling [60,61]. These data suggest a possible role for
436 *Sertad4* in Wnt signaling.
437
438 Despite their clinical importance, we know little about the genetics of bone traits other
439 than BMD. Here, we set out to address this knowledge gap. Using the DO, we identified
440 28 QTL for a wide-range of complex bone traits. The QTL were mapped at high-
441 resolution, most had 95% CIs < 1 Mbp [18]. This precision, coupled with merge and eQTL
442 analyses, allowed us to identify a small number of candidate genes for many loci.
443 Overlap of existing human BMD GWAS association and mouse loci was no more than
444 what would be expected by chance, suggesting that our approach has highlighted
445 biological processes impacting bone that are independent of those with the largest
446 effects on BMD. This new knowledge has the potential to lead to novel pathways which
447 could be targeted therapeutically to increase bone strength. Future studies extending
448 the work presented here will lead to the identification of additional genes and further our
449 understanding of genetics of a broad range of complex skeletal traits.
450
451 Disulfide bonds are critical to the structure and function of numerous proteins [62]. Most
452 disulfide bonds are formed in the endoplasmic reticulum [63]; however, the discovery of
453 QSOX1 demonstrated that disulfide bonds in proteins can be formed extracellularly [57].
454 Ilani *et al*. [57] demonstrated that fibroblasts deficient in QSOX1 had a decrease in the
455 number of disulfide bonds in matrix proteins. Moreover, the matrix formed by these cells

456 was defective in supporting cell-matrix adhesion and lacked incorporation of the alpha-4
457 isoform of laminin. QSOX1 has also been associated with perturbation of the
458 extracellular matrix in the context of cancer and tumor invasiveness [64,65]. It is unclear at
459 this point how QSOX1 influences cortical bone mass; however, it likely involves
460 modulation of the extracellular matrix.
461
462 In summary, we have used a systems genetics analysis in DO mice to inform human
463 GWAS and identify novel genetic determinants for a wide-range of complex skeletal
464 traits. Through the use of multiple synergistic approaches, we have expanded our
465 understanding of the genetics of BMD and osteoporosis. This work has the potential to
466 serve as a framework for how to use the DO, and other mouse genetic reference
467 populations, to complement and inform human genetic studies of complex disease.
468

Acknowledgements:

Research reported in this publication was supported in part by the National Institute of Arthritis and Musculoskeletal and Skin Diseases of the National Institutes of Health under Award Number AR057759 to C.J.R., M.C.H., and C.R.F. B.A-B was supported in part by a National Institutes of Health, Biomedical Data Sciences Training Grant (5T32LM012416). The authors acknowledge Wenhao Xu (University of Virginia) and the Genetically Engineered Mouse Models (GEMM) core and the University of Virginia Cancer Center Support Grant (CCSG) P30CA044579 from NCI for their support generating *Qsox1* mutant mice. The authors also acknowledge the Yale School of Medicine Department of Orthopaedics and Rehabilitation's Histology and Histomorphometry Laboratory for all their work. We thank Matt Vincent (The Jackson Laboratory) and Gary Churchill (The Jackson Laboratory) for developing the QTL Viewer software and Neal Magee (University of Virginia) for hosting QTL Viewer on UVA servers. We thank the IMPC for accessibility to BMD data on *Glt8d2* knockout mice (www.mousephenotype.org). The data used for the analyses described in this manuscript were obtained from the IMPC Portal on 11/5/19. The Genotype-Tissue Expression (GTEx) Project was supported by the Common Fund of the Office of the Director of the National Institutes of Health, and by NCI, NHGRI, NHLBI, NIDA, NIMH, and NINDS. The data used for the analyses described in this manuscript were obtained from the GTEx Portal on 01/15/18.

METHODS:

Diversity Outbred mouse population and tissue harvesting: A total of 619 (315 males, 304 females) Diversity Outbred (J:DO, JAX stock #0039376) mice, across 11 generations (gens. 23-33) were procured from The Jackson Laboratory at 4 weeks of age. DO mice were fed standard chow, and were injected with calcein (30 mg/g body weight) both 7 days and 1 day prior to sacrifice. Mice were weighed and fasted 24 hours prior to sacrifice. Mice were sacrificed at approximately 12 weeks of age (mean: 12.4 weeks). Immediately prior to sacrifice, mice were anesthetized with isoflurane, nasal-anal length was recorded and blood collected via submandibular bleeding. At sacrifice, femoral morphology (length and width) was measured with digital calipers (Mitoyuto American, Aurora, IL). Right femora were wrapped in PBS soaked gauze and stored in PBS at -20°C. Right tibiae were stored in 70% EtOH at room temperature. Left femora were flushed of bone marrow (which was snap frozen and stored in liquid nitrogen, see below – Single cell RNA-seq of bone marrow stromal cells) and were immediately homogenized in Trizol. Homogenates were stored at -80°C. Left tibiae were stored in 10% neutral buffered formalin at 4°C. Tail clips were collected and stored at -80°C.

Measurement of trabecular and cortical microarchitecture: Right femora were scanned using a 10 µm isotropic voxel size on a desktop µCT40 (Scanco Medical AG, Brüttisellen, Switzerland), following the Journal of Bone and Mineral Research guidelines for assessment of bone microstructure in rodents [66]. Trabecular bone architecture was analyzed in the endocortical region of the distal metaphysis. Variables computed for trabecular bone regions include: bone volume, BV/TV, trabecular number,

thickness, separation, connectivity density and the structure model index, a measure of the plate versus rod-like nature of trabecular architecture. For cortical bone at the femoral midshaft, total cross-sectional area, cortical bone area, medullary area, cortical thickness, cortical porosity and area moments of inertia about principal axes were computed.

Biomechanical testing: The right femur from each mouse was loaded to failure in four-point bending in the anterior to posterior direction, such that the posterior quadrant is subjected to tensile loads. The widths of the lower and upper supports of the four-point bending apparatus are 7 mm and 3 mm, respectively. Tests were conducted with a deflection rate of 0.05 mm/s using a servohydraulic materials test system (Instron Corp., Norwood, MA). The load and mid-span deflection were acquired directly at a sampling frequency of 200 Hz. Load-deflection curves were analyzed for strength (maximum load), stiffness (the slope of the initial portion of the curve), post-yield deflection, and total work. Post-yield deflection, which is a measure of ductility, is defined as the deflection at failure minus the deflection at yield. Yield is defined as a 10% reduction of stiffness relative to the initial (tangent) stiffness. Work, which is a measure of toughness, is defined as the area under the load-deflection curve. Femora were tested at room temperature and kept moist with phosphate buffered saline during all tests.

Assessment of bone marrow adipose tissue (MAT): Fixed right tibiae, dissected free of soft tissues, were decalcified in EDTA for 20 days, changing the EDTA every 3-4 days and stained for lipid using a 1:1 mixture of 2% aqueous osmium tetroxide (OsO_4)

and 5% potassium dichromate. Decalcified bones were imaged using µCT performed in water with energy of 55 kVp, an integration time of 500 ms, and a maximum isometric voxel size of 10 µm (the “high” resolution setting with a 20mm sample holder) using a µCT35 (Scanco). To determine the position of the MAT within the medullary canal and to determine its change in volume, the bone was overlaid. MAT was recorded in 4 dimensions.

Histomorphometry: Fixed right tibiae were sequentially dehydrated and infiltrated in graded steps with methyl methacrylate. Blocks were faced and 5 µm non-decalcified sections cut and stained with toludine blue to observe gross histology. This staining allows for the observation of osteoblast and osteoclast numbers, amount of unmineralized osteoid and the presence of mineralized bone. Histomorphometric parameters were analyzed on a computerized tablet using Osteomeasure software (Osteometrics, Atlanta, GA). Histomorphometric measurements were made on a fixed region just below the growth plate corresponding to the primary spongiosa.

RNA isolation, sequencing and quantification: Total RNA was isolated from marrow-depleted homogenates of the left femora, using the mirVana™ miRNA Isolation Kit (Life Technologies, Carlsbad, CA). Total RNA-Seq libraries were constructed using Illumina TruSeq Stranded Total RNA HT sample prep kits. Samples were sequenced to an average of 39 million 2 x 75 bp paired-end reads (total RNA-seq) on an Illumina NextSeq500 sequencer in the University of Virginia Center for Public Health Genomics Genome Sciences Laboratory (GSL). A custom bioinformatics pipeline was used to

559 quantify RNA-seq data. Briefly, RNA-seq FASTQ files were quality controlled using
560 FASTQC [67], aligned to the mm10 genome assembly with HISAT2 [68], and quantified with
561 Stringtie [69]. Read count information was then extracted with a Python script provided by
562 the Stringtie website (prepDE.py). Finally, we filtered our gene set to include genes that
563 had more than 6 reads, and more than 0.1 transcripts per million (TPM), in more than
564 38 samples (20% of all samples). Sequencing data is available on GEO (GSE152708).
565
566 **Mouse genotyping:** DNA was collected from mouse tails using the PureLink Genomic
567 DNA mini kit (Invitrogen)**.** DNA was used for genotyping with the GigaMUGA array [19] by
568 Neogen Genomics (GeneSeek; Lincoln, NE). Genotyping reports were pre-processed
569 for use with the qtl2 R package [70] [71] , and genotypes were encoded using directions and
570 scripts from (kbroman.org/qtl2/pages/prep_do_data.html). Quality control was
571 performed using the Argyle R package [72], where samples were filtered to contain no
572 more than 5% no calls and 50% heterozygous calls. Samples that failed QC were re-
573 genotyped. Furthermore, genotyping markers were filtered to contain only tier 1 and tier
574 2 markers. Markers that did not uniquely map to the genome were also removed.
575 Finally, a qualitative threshold for the maximum number of no calls and a minimum
576 number of homozygous calls was used to filter markers.

577 We calculated genotype and allele probabilities, as well as kinship matrices using the
578 qtl2 R package. Genotype probabilities were calculated using a hidden Markov model
579 with an assumed genotyping error probability of 0.002, using the Carter-Falconer map
580 function. Genotype probabilities were then reduced to allele probabilities, and allele
581 probabilities were used to calculate kinship matrices, using the “leave one chromosome

582 out" (LOCO) parameter. Kinship matrices were also calculated using the "overall"
583 parameter for heritability calculations.

584 Further quality control was then performed [73], which led to the removal of several
585 hundred more markers that had greater than 5% genotyping errors, after which
586 genotype and allele probabilities and kinship matrices were recalculated. As another
587 metric for quality control, we calculated the frequencies of the eight founder genotypes
588 of the DO.

589

590 **WGCNA network construction:** Gene counts, as obtained above were pruned to
591 remove genes that had fewer than 10 reads in more than 90% of samples. Variance
592 stabilizing transformation (DeSeq2 [74]) was applied, followed by RNA-seq batch
593 correction using sex and age at sacrifice in days as covariates, using ComBat ("sva" R
594 package [75]). We then used the "WGCNA" R package to generate signed co-expression
595 networks with a soft thresholding power of 4 (power=5 for male networks) [76,77]. We used
596 the "blockwiseModules" function to construct networks with a merge cut height of 0.15
597 and minimum module size of 30. WGCNA networks had 39, 45 and 40 modules for the
598 sex-combined, female and male networks, respectively.

599 **Bayesian network learning**: Bayesian networks for each WGCNA module were
600 learned with the "bnlearn" R package [78]. Specifically, expression data for genes within a
601 WGCNA module was obtained as above (WGCNA network construction), and these
602 data were used to learn the structure of the underlying Bayesian network using the Max-
603 Min Hill Climbing algorithm (function "mmhc" in bnlearn).

Construction of "known bone gene" list: We constructed a list of bone genes using Gene Ontology (GO) terms and the Mouse Genome Informatics (MGI) database [79 80]. Using AmiGO2, we downloaded GO terms for "osteo*", "bone" and "ossif*" [81]. The resulting GO terms were pruned to remove some terms that were not related to bone function or regulation. We then used the MGI data table to convert human genes to their mouse homologs. We also downloaded human and mouse genes from MGI which had the terms "osteoporosis", "bone mineral density", "osteoblast", "osteoclast", and "osteocyte". Human genes were converted to their mouse counterparts as above. GO and MGI derived genes were merged and duplicates were removed, resulting in the known bone gene set.

Bone Associated Node (BAN) analysis: We used a custom script that utilized the "igraph" R package to perform BAN analysis [82]. Briefly, within a Bayesian network underlying a WGCNA module, we counted the number of neighbors for each gene, based on a neighborhood step size of 3. Neighborhood sizes also included the gene itself. BANs were defined as genes that were more highly connected to bone genes than would be expected by chance. We merged all genes from all BNs together in a matrix, and removed genes that were unconnected or only connected to 1 neighbor (neighborhood size <=2). We then pruned all genes whose neighborhood size was greater than 1 standard deviation less than the mean neighborhood size across all modules.

Then, for each gene, we calculated if they were more connected to bone genes in our bone list (see construction of bone list above) than expected by chance using the hypergeometric distribution (phyper, R "stats" package). The arguments were as

follows: q: (number of genes in neighborhood that are also bone genes) – 1; m: total number of bone genes in our bone gene set; n: (number of genes in networks prior to pruning) – m; k: neighborhood size of the respective gene; lower.tail = false. False discovery rates were calculated using p.adjust().

GWAS-eQTL colocalization: We converted mouse genes with evidence of being a BAN (P<=0.05) to their human homologs using the MGI homolog data table. If the human homolog was within 1Mbp of a GWAS association, we obtained all eQTL associations within +/- 200 kb of the GWAS association in all 48 tissues of version 7 of the Gene-Tissue Expression Project (GTEx). These variants were overlapped with the GWAS variants, and colocalization was performed using the R "coloc" package, using the coloc.abf() function [83]. Genes were considered colocalizing if PPH4 >= 0.75.

Gene ontology: Gene ontology analysis for WGCNA modules was performed for each individual module using the "topGO" package in R [84]. Enrichment tests were performed for the "Molecular Function", "Biological Process" and "Cellular Component" ontologies, using all genes in the network. Enrichment was performed using the "classic" algorithm with Fisher's exact test. P-values were not corrected for multiple testing.

Assessing the expression of *Glt8d2* and *Sertad4* in publicly available bone cell data: We used bioGPS expression data from GEO (GSE10246) to assay the expression of *Sertad4*, *Glt8d2,* and *Qsox1* in osteoblasts and osteoclasts[45]. We also downloaded the data from GEO (GSE54461) to query expression in primary calvarial osteoblasts.

649 **Analysis of BMD data on *Rasd1*$^{-/-}$ mice from the IMPC:** The International Mouse
650 Knockout Consortium [55] and the IMPC[85] have generated and phenotyped mice
651 harboring null alleles for *Glt8d2* (*Glt8d2*$^{tm1a(KOMP)Wtsi}$,*Gltd2*$^{-/-}$) (N=7 females and N=7
652 males). Phenotypes for the appropriate controls (C57BL/6) were also collected
653 (N=1,466 females and N=1,477 males). A description of the battery of phenotypes
654 collected on mutants can be found at
655 (https://www.mousephenotype.org/impress/PipelineInfo?id=4). The mice were 14
656 weeks of age at DEXA scanning and both sexes for both mutants were included. We
657 downloaded raw BMD, body weight and metadata for *Glt8d2* mutants from the IMPC
658 webportal (http://www.mousephenotype.org). These data were analyzed using the
659 PhenStat R package [86]. PhenStat was developed to analyze data generated by the
660 IMPC in which a large number of wild-type controls are phenotyped across a wide-time
661 range in batches and experimental mutant animals are tested in small groups
662 interspersed among wild-type batches. We used the Mixed Model framework in
663 PhenStat to analyze BMD data. The mixed model framework starts with a full model
664 (with fixed effects of genotype, sex, genotype x sex and weight and batch as a random
665 effect) and ends with final reduced model and genotype effect evaluation procedures
666 [86,87].

667 **QTL mapping:** Phenotypes that notably deviated from normality were $\log_{10}$-transformed
668 (the MAT phenotypes as well as PYD and W_{py} were transformed after a constant of 1
669 was added). Then, QTL mapping with a single-QTL model was performed via a linear
670 mixed model using the “scan1” function of the “qtl2” R package. A kinship matrix as
671 calculated by the “leave one chromosome out” method was included. Mapping

672 covariates were sex, age at sacrifice in days, bodyweight, and DO mouse generation.
673 Peaks were then identified with a minimum LOD score of 4 and a peak drop of 1.5
674 LODs. To identify significant QTL peaks, we permuted each phenotype scan 1000 times
675 (using the “scan1perm” function of the “qtl2” package) with the same mapping
676 covariates as above, and calculated the significance threshold for each phenotype at a
677 5% significance level. Heritability for the phenotypes was calculated using the
678 “est_herit” function of the “qtl2” R package, using the same covariates as above, but
679 with a kinship matrix that was calculated using the “overall” argument.

680 **eQTL mapping:** Variance stabilizing transformation was applied to gene read counts
681 from above using the “DESeq2” R package, followed by quantile-based inverse Normal
682 transformation[88]. Then, hidden determinants of gene expression were calculated from
683 these transformed counts, using Probabilistic Estimation of Expression Residuals
684 (PEER)[89]. 48 PEER factors were calculated using no intercept or covariates. Sex and
685 the 48 PEER covariates were used as mapping covariates, and eQTL mapping was
686 performed using the “scan1” function, as above. To calculate a LOD score threshold, we
687 randomly chose 50 genes and permuted them 1000 times, as above. Since all genes
688 were transformed to conform to the same distribution, we found that using 50 was
689 sufficient. Thresholds were set as the highest permuted LOD score each for autosomal
690 chromosomes and the X-chromosome (10.89 and 11.55 LODs, respectively). Finally,
691 we identified peaks as above, and defined eQTL as peaks that exceeded the LOD
692 threshold and were no more than 1Mbp away from their respective transcript’s start site,
693 as defined by the Stringtie output.

Merge analysis: For each QTL or eQTL peak, we imputed all variants within the 95% confidence interval of a peak, and tested each variant for association with the respective trait. This was performed using the "scan1snps" function of the "qtl2" R package, with the same mapping covariates for QTL or eQTL, respectively. Then, we identified "top" variants by taking variants that were within 85% of the maximum SNP association's LOD score. For conditional analyses using a variant, we performed the same QTL scan as above, but included the genotype of the respective SNP as an additive mapping covariate, encoding it as a 0, 0.5 or 1, for homozygous alternative, heterozygous or homozygous reference, respectively.

BMD GWAS overlap: To identify BMD GWAS loci that overlapped with our DO mouse associations, we defined a mouse association locus as the widest confidence interval given all QTL start and end CI positions mapping to each locus. We then used the UCSC liftOver tool [90] (minimum ratio of bases that must remap = 0.1, minimum hit size in query = 100000) to convert the loci from mm10 to their syntenic hg19 positions. We then took all genome-wide significant SNPs (P.NI <=5 x 10^{-8}) from the Morris GWAS for eBMD, and identified variants that overlapped with the syntenic mouse loci ("GenomicRanges" R package [91]).

SIFT annotations: SIFT annotations for merge analysis missense variants were queried using Ensembl's Variant Effect Predictor tool (https://useast.ensembl.org/Tools/VEP) [92]. All options were left as default.

Prior ML QTL mapping: The cohorts used for the earlier QTL mapping of ML consisted of 577 Diversity Outbred mice from breeding generations G10 and G11 [93]. G10 cohort

mice consisted of both males and females fed a standard chow diet, and were euthanized and analyzed at 12–15 weeks of age. G11 cohort mice were all females fed either a high-fat, cholesterol-containing (HFC) diet or a low-fat, high protein diet, and were euthanized and analyzed at 24–25 weeks of age. Mice were weighed and then euthanized by CO_2 asphyxiation followed by cervical dislocation. Carcasses were frozen at -80°C. Subsequently, the femur was dissected and length, AP width, and ML width was measured two independent times to 0.01 mm using digital calipers. Mice were genotyped using the MegaMUGA SNP array (GeneSeek; Lincoln, NE) designed with 77,800 SNP markers, and QTL mapping was performed as above, but with the inclusion of sex, diet, age and weight at sacrifice as additive covariates.

Generation of *Qsox1* mutant mice: *Qsox1* knockout mice used in this study were generated using the CRISPR/Cas9 genome editing technique essentially as reported in [94]. *Qsox1* knockout mice used in this study were generated using the CRISPR/Cas9 genome editing technique essentially as reported in [94]. Briefly, Cas9 enzyme that was injected into B6SJLF2 embryos (described below) was purchased from (PNA Bio) while the guide RNA (sgRNA) was designed and synthesized as follows: the 20 nucleotide (nt) sequence that would be used to generate the sgRNA was chosen using the CRISPR design tool developed by the Zhang lab (crispr.mit.edu). The chosen sequence and its genome map position is homologous to a region in Exon 1 that is ~225 bp, 3' of the translation start site and ~20bp 5' of the Exon1/Intron1 boundary (**Supplemental Table 15**). To generate the sgRNA that would be used for injections oligonucleotides of the chosen sequence, as well as the reverse complement (**Supplemental Table 15**), primers 1 and 2, respectively), were synthesized such that an additional 4 nts (CACC

and AAAC) were added at the 5' ends of the oligonucleotides for cloning purposes. These oligonucleotides were annealed to each other by combining equal molar amounts, heating to 90°C for 5 min. and allowing the mixture to passively cool to room temperature. The annealed oligonucleotides were combined with BbsI digested pX330 plasmid vector (provided by the Zhang lab through Addgene; https://www.addgene.org/) and T4 DNA ligase (NEB) and subsequently used to transform Stbl3 competent bacteria (Thermo Fisher) following the manufacturer's' protocols. Plasmid DNAs from selected clones were sequenced from primer 3 (**Supplemental Table 15**) and DNA that demonstrated accurate sequence and position of the guide were used for all downstream applications. The DNA template used in the synthesis of the sgRNA was the product of a PCR using the verified plasmid DNA and primers 4 and 5 (**Supplemental Table 15**). The sgRNA was synthesized via *in vitro* transcription (IVT) by way of the MAXIscript T7 kit (Thermo Fisher) following the manufacturer's protocol. sgRNAs were purified and concentrated using the RNeasy Plus Micro kit (Qiagen) following the manufacturer's protocol.

B6SJLF1 female mice (Jackson Laboratory) were super-ovulated and mated with B6SJLF1 males. The females were sacrificed and the fertilized eggs (B6SJLF2 embryos) were isolated from the oviducts. The fertilized eggs were co-injected with the purified Cas9 enzyme (50 ng/µl) and sgRNA (30 ng/µl) under a Leica inverted microscope equipped with Leitz micromanipulators (Leica Microsystems). Injected eggs were incubated overnight in KSOM-AA medium (Millipore Sigma). Two-cell stage embryos were implanted on the following day into the oviducts of pseudo pregnant ICR

762 female mice (Envigo). Pups were initially screened by PCR of tail DNA using primers 6
763 and 7 with subsequent sequencing of the resultant product from primer 8, when the
764 PCR products suggested a relatively large deletion had occurred in at least one of the
765 alleles (**Supplemental Table 15**). For those samples which indicated a small or no
766 deletion had occurred PCR of tail DNA using primers 9 and 10 was performed with
767 subsequent sequencing of the resultant products from primer 11 (**Supplemental Table**
768 **15**). Finally, deletions were fully characterized by ligating, with T4 DNA ligase (NEB),
769 the PCR products from either primer pairs 6/7 or 9/10 with the plasmid vector pCR 2.1
770 (Thermo Fisher) followed by transformation of One Shot Top 10 chemically competent
771 cells (Thermo Fisher) following the manufacturers recommendations (**Supplemental**
772 **Tables 13 and 14**).

773 The resulting founder mice (see **Supplemental Table 13**) were mated to C57BL/6J
774 mice (Jackson Laboratory), with CRISPR/Cas9-deletion heterozygous F1 offspring from
775 the 1st and 2nd litters mated to generate the F2 offspring used in the study of bone
776 related properties reported herein. In addition, mouse B (**Supplemental Table 13**) was
777 subsequently mated to an SJL/J male (Jackson Laboratory), and the F2 offspring from
778 the heterozygous F1 crosses, as outlined above, were also used in this study. All F1
779 and F2 mice from all deletion 'strains' were genotyped using primer pairs 9/10, with the
780 PCR products sequenced from primer 11 for mice possessing the 7+6 and 1bp
781 deletions (**Supplemental Table 15**). An additional PCR using primers 6 and 7 was
782 performed with tail DNA from mice carrying the 1347 bp and 756 bp deletions; the
783 products from this 2nd PCR assisted in determining between heterozygous and
784 homozygous deleted genotypes (**Supplemental Table 15**).

ML was measured for both femurs using calipers on a population of F2 mice and ML was averaged between the two femurs. A linear model with genotype, mutation type, length, and weight was generated separately for males and females. Lsmeans were calculated using the "emmeans" R package [95].

We randomly selected 50 male F2 mice (25 wt + 25 mut) from the same population, and microarchitectural phenotypes were measured as above, but on left femurs. Bone strength was measured as above but in both the AP and ML orientations. A linear model with genotype, mutation type and weight was generated, and lsmeans were calculated using the "emmeans" R package[95].

Measuring Qsox1 activity in serum: Serum was collected via submandibular bleeding from isoflurane anesthetized mice, prior to sacrifice and isolation of femurs for bone trait analysis. Blood samples were incubated at room temperature for 20-30 m followed by centrifugation at 2000 x g for 10 m at 4°C. The supernatants were transferred to fresh tubes and centrifuged again as described above. The 2nd supernatant of each sample was separated into 50-100 µl aliquots, snap frozen on dry ice and stored at -70°C. Only 'clear' serum samples were used for determining QSOX1 activity, because pink-red colored samples had slight-moderate activity, presumably due to sulfhydryl oxidase enzymes released from lysed red blood cells.

Sulfhydryl oxidase activity was determined as outlined in Israel *et al.*, 2014 [96] with minor modifications. Briefly, serum samples were thawed on wet ice whereupon 5 µl was used in a 200 µl final reaction volume which consisted of 50 mM KPO_4, pH7.5, 1mM EDTA (both from Sigma), 10 µM Amplex UltraRed (Thermo Fisher), 0.5% (v/v) Tween

80 (Surfact-Amps, low peroxide; Thermo Fisher), 50 nM Horseradish Peroxide (Sigma), and initiated with the addition of dithiothreitol (Sigma) to 50 µM initial concentration. The reactions were monitored with the 'high-sensitive dsDNA channel' of a Qubit Fluorimeter (Thermo Fisher) by measuring the fluorescence every 15-30s for 10m. The assay was calibrated by adding varying concentrations (0-3.2 µM) of freshly diluted H_2O_2 (Sigma) to the reaction mixture minus serum. Enzyme activity was expressed in units of (pmol H_2O_2/min/µl serum) and typically calculated within the first several minutes of the reaction for wild-type and heterozygous mutant mice. It was calculated using the entire 10m of the reaction for homozygous mutant genotypes.

Single cell RNA-seq of bone marrow stromal cells:

Bone marrow isolation: The left femur was isolated and cleaned thoroughly of all muscle tissue followed by removal of its distal epiphysis. The marrow was exuded by centrifugation at 2000 x g for 30 seconds into a sterile tube containing 35 µl freezing media (90% FBS, 10% DMSO). The marrow was then triturated 6 times on ice after addition of 150 µl ice cold freezing media and again after further addition of 1ml ice cold freezing media until no visible clumps remained prior to being placed into a Mr. Frosty Freezing Container (Thermo Scientific) and stored overnight at -80^{o} C. Samples were transferred the following day to liquid nitrogen for long term storage.

Bone marrow culturing: Previously frozen bone marrow samples were thawed at 37^{o} C, resuspended into 5 ml bone marrow growth media (Alpha MEM, 10% FBS, 1% Pen/Strep, 0.01% Glutamax), pelleted in a Sorvall tabletop centrifuge at 1000 rpm for 5

minutes at room temperature and then subjected to red blood cell lysis by resuspending and triturating the resultant pellet into 5 ml 0.2% NaCl for 20 seconds, followed by addition and thorough mixing of 1.6% NaCl. Cells were pelleted again, resuspended into 1 ml bone marrow growth media, plated into one well per sample of a 48 well tissue culture plate and placed into a 37^{o} C, 5% CO_2 incubator undisturbed for 3 days post-plating, at which time the media was aspirated, cells were washed with 1 ml DPBS once and bone marrow growth media was replaced at 300 µl volume. The was process was repeated through day 5 post-plating. At day 6 post-plating, cells were washed in same manner; however, bone marrow growth media was replaced with 300 µl bone marrow differentiation media (Alpha MEM, 10% FBS, 1% Penicillin Streptomycin, 0.01% Glutamax, 50mg/ml Ascorbic Acid, 1M B-glycerophosphate, 100uM Dexamethasome). Cultures were then washed in same manner every other day for the following 10 days.

RNA isolation: The isolation procedure outlined below was inspired by Hanna *et al*.[97] Mineralized cultures were washed twice with Dulbecco's Phosphate Buffered Saline (DPBS). 0.5ml 60mM EDTA (pH 7.4, made in DPBS) was added for 15-minute room temperature (RT) incubation. EDTA solution was aspirated and replaced for a second 15-minute RT incubation. Cultures were then washed with 0.5ml Hank's Balanced Salt Solution (HBSS) and incubated with 0.5ml 8mg/ml collagenase in HBSS/4mM $CaCl_2$ for 10 minutes at 37^{o} C with shaking. Cultures were triturated 10x and incubated for an additional 20 minutes and 37º C. Cultures were then transferred to a 1.5ml Eppendorf tube, and spun at 500 x g for 5 minutes at RT in a Sorvall tabletop centrifuge. Cultures were resuspended in 0.5ml 0.25% trypsin-EDTA (Gibco, Gaithersburg, MD) and

incubated for 15 minutes at 37^{o} C. Cultures were then triturated and incubated for an additional 15 minutes. 0.5ml of media were added, triturated and spun at 500 x g for 5 minutes at RT. Cultures were then resuspended in 0.5ml bone marrow differentiation media and cells were counted.

Library preparation, sequencing and analysis: The samples were pooled and concentrated to 800 cells/µl in sterile PBS supplemented with 0.1% BSA. The single cell suspension was loaded into a 10x Chromium Controller (10X Genomics, Pleasanton, CA, USA), aiming to capture 8,000 cells, with the Single Cell 3' v2 reagent kit, according to the manufacturer's protocol. Following GEM capturing and lysis, cDNA was amplified (13 cycles) and the manufacturer's protocol was followed to generate sequencing library. The library was sequenced on the Illumina NextSeq500 and the raw sequencing data was processed using CellRanger toolkit (version 2.0.1). The reads were mapped to mm10 mouse reference genome assembly using STAR (version 2.5.1b) [98]. Sequencing data is available on GEO (GSE152806).

Analysis was performed using Seurat [99,100]. Features detected in at least 3 cells where at least 200 features were detected were used. We then filtered out cells with less than 800 reads and more than 5800 reads, as well as cells with 10% or more mitochondrial reads. Expression measurements were multiplied by 10,000 and log normalized, and the 3000 most variable features were identified. The data were then scaled. Cells were then scored by cell cycle markers, and these scores, as well as the percentage of mitochondrial reads, were regressed out [101]. Finally, clusters were found with a

resolution of 1 and the UMAP was generated. An outlier cluster consisting of 13 cells was removed.

Data availability:

Code is available at https://github.com/basel-maher/DO_project. Genotype probabilities, phenotypic data, trait QTL, and eQTL are available at http://qtlviewer.uvadcos.io/. Raw sequencing data is available from the NCBI Gene Expression Omnibus database (GSE152708, GSE152806). Raw genotyping data is available upon request.

886 **REFERENCES:**

887 1. Black, D. M. & Rosen, C. J. Clinical Practice. Postmenopausal Osteoporosis. *N. Engl. J.*
888 *Med.* **374**, 254–262 (2016).
889 2. Burge, R. *et al.* Incidence and economic burden of osteoporosis-related fractures in the
890 United States, 2005-2025. *J. Bone Miner. Res.* **22**, 465–475 (2007).
891 3. Estrada, K. *et al.* Genome-wide meta-analysis identifies 56 bone mineral density loci and
892 reveals 14 loci associated with risk of fracture. *Nat. Genet.* **44**, 491–501 (2012).
893 4. Kemp, J. P. *et al.* Identification of 153 new loci associated with heel bone mineral density
894 and functional involvement of GPC6 in osteoporosis. *Nat. Genet.* **49**, 1468–1475 (2017).
895 5. Morris, J. A. *et al.* An atlas of genetic influences on osteoporosis in humans and mice. *Nat.*
896 *Genet.* **51**, 258–266 (2019).
897 6. Richards, J. B., Zheng, H.-F. & Spector, T. D. Genetics of osteoporosis from genome-wide
898 association studies: advances and challenges. *Nat. Rev. Genet.* **13**, 576–588 (2012).
899 7. Sabik, O. L. & Farber, C. R. Using GWAS to identify novel therapeutic targets for
900 osteoporosis. *Transl. Res.* **181**, 15–26 (2017).
901 8. Nadeau, J. H. & Dudley, A. M. Genetics. Systems genetics. *Science* **331**, 1015–1016
902 (2011).
903 9. Civelek, M. & Lusis, A. J. Systems genetics approaches to understand complex traits. *Nat.*
904 *Rev. Genet.* **15**, 34–48 (2014).
905 10. GTEx Consortium *et al.* Genetic effects on gene expression across human tissues. *Nature*
906 **550**, 204–213 (2017).
907 11. Al-Barghouthi, B. M. & Farber, C. R. Dissecting the Genetics of Osteoporosis using
908 Systems Approaches. *Trends Genet.* **35**, 55–67 (2019).
909 12. Dufresne, T. E., Chmielewski, P. A., Manhart, M. D., Johnson, T. D. & Borah, B.
910 Risedronate preserves bone architecture in early postmenopausal women in 1 year as
911 measured by three-dimensional microcomputed tomography. *Calcif. Tissue Int.* **73**, 423–

912 432 (2003).

913 13. Cummings, S. R. *et al.* Improvement in spine bone density and reduction in risk of vertebral
914 fractures during treatment with antiresorptive drugs. *Am. J. Med.* **112**, 281–289 (2002).

915 14. Lochmüller, E.-M. *et al.* Correlation of Femoral and Lumbar DXA and Calcaneal Ultrasound,
916 Measured In Situ with Intact Soft Tissues, with the In Vitro Failure Loads of the Proximal
917 Femur. *Osteoporosis International* vol. 8 591–598 (1998).

918 15. Melton, L. J., III, Chrischilles, E. A., Cooper, C., Lane, A. W. & Riggs, B. L. How Many
919 Women Have Osteoporosis? *J. Bone Miner. Res.* **20**, 886–892 (2005).

920 16. Churchill, G. A., Gatti, D. M., Munger, S. C. & Svenson, K. L. The Diversity Outbred mouse
921 population. *Mamm. Genome* **23**, 713–718 (2012).

922 17. Logan, R. W., Robledo, R. F. & Recla, J. M. High-precision genetic mapping of behavioral
923 traits in the diversity outbred mouse population. *Genes Brain Behav.* (2013).

924 18. Svenson, K. L. *et al.* High-resolution genetic mapping using the Mouse Diversity outbred
925 population. *Genetics* **190**, 437–447 (2012).

926 19. Morgan, A. P. *et al.* The Mouse Universal Genotyping Array: From Substrains to
927 Subspecies. *G3* **6**, 263–279 (2015).

928 20. Karasik, D. *et al.* Heritability and Genetic Correlations for Bone Microarchitecture: The
929 Framingham Study Families. *J. Bone Miner. Res.* **32**, 106–114 (2017).

930 21. Ng, A. H. M., Wang, S. X., Turner, C. H., Beamer, W. G. & Grynpas, M. D. Bone quality and
931 bone strength in BXH recombinant inbred mice. *Calcif. Tissue Int.* **81**, 215–223 (2007).

932 22. Turner, C. H. *et al.* Variation in bone biomechanical properties, microstructure, and density
933 in BXH recombinant inbred mice. *J. Bone Miner. Res.* **16**, 206–213 (2001).

934 23. Schlecht, S. H. & Jepsen, K. J. Functional integration of skeletal traits: an intraskeletal
935 assessment of bone size, mineralization, and volume covariance. *Bone* **56**, 127–138
936 (2013).

937 24. Zhang, B. & Horvath, S. A general framework for weighted gene co-expression network

938 analysis. *Stat. Appl. Genet. Mol. Biol.* **4**, Article17 (2005).

939 25. Watson, C. T. *et al.* Integrative transcriptomic analysis reveals key drivers of acute peanut
940 allergic reactions. *Nat. Commun.* **8**, 1943 (2017).

941 26. Huan, T. *et al.* Integrative network analysis reveals molecular mechanisms of blood
942 pressure regulation. *Mol. Syst. Biol.* **11**, 799 (2015).

943 27. Wang, I.-M. *et al.* Systems analysis of eleven rodent disease models reveals an
944 inflammatome signature and key drivers. *Mol. Syst. Biol.* **8**, 594 (2012).

945 28. Mäkinen, V.-P. *et al.* Integrative genomics reveals novel molecular pathways and gene
946 networks for coronary artery disease. *PLoS Genet.* **10**, e1004502 (2014).

947 29. Aguet, F. *et al.* The GTEx Consortium atlas of genetic regulatory effects across human
948 tissues. *bioRxiv* 787903 (2019) doi:10.1101/787903.

949 30. Aguet, F. *et al.* Local genetic effects on gene expression across 44 human tissues. *bioRxiv*
950 074450 (2016) doi:10.1101/074450.

951 31. Nakashima, K. *et al.* The novel zinc finger-containing transcription factor osterix is required
952 for osteoblast differentiation and bone formation. *Cell* **108**, 17–29 (2002).

953 32. Balemans, W. *et al.* Increased bone density in sclerosteosis is due to the deficiency of a
954 novel secreted protein (SOST). *Hum. Mol. Genet.* **10**, 537–543 (2001).

955 33. Brunkow, M. E. *et al.* Bone dysplasia sclerosteosis results from loss of the SOST gene
956 product, a novel cystine knot-containing protein. *Am. J. Hum. Genet.* **68**, 577–589 (2001).

957 34. Gong, Y. *et al.* LDL receptor-related protein 5 (LRP5) affects bone accrual and eye
958 development. *Cell* **107**, 513–523 (2001).

959 35. Little, R. D. *et al.* A mutation in the LDL receptor-related protein 5 gene results in the
960 autosomal dominant high-bone-mass trait. *Am. J. Hum. Genet.* **70**, 11–19 (2002).

961 36. Boyden, L. M. *et al.* High bone density due to a mutation in LDL-receptor-related protein 5.
962 *N. Engl. J. Med.* **346**, 1513–1521 (2002).

963 37. Kong, Y. Y. *et al.* OPGL is a key regulator of osteoclastogenesis, lymphocyte development

964 and lymph-node organogenesis. *Nature* **397**, 315–323 (1999).

965 38. Wong, B. R. *et al.* TRANCE (Tumor Necrosis Factor [TNF]-related Activation-induced
966 Cytokine), a New TNF Family Member Predominantly Expressed in T cells, Is a Dendritic
967 Cell–specific Survival Factor. *Journal of Experimental Medicine* vol. 186 2075–2080 (1997).

968 39. Yasuda, H. *et al.* Osteoclast differentiation factor is a ligand for
969 osteoprotegerin/osteoclastogenesis-inhibitory factor and is identical to TRANCE/RANKL.
970 *Proc. Natl. Acad. Sci. U. S. A.* **95**, 3597–3602 (1998).

971 40. Lacey, D. L. *et al.* Osteoprotegerin ligand is a cytokine that regulates osteoclast
972 differentiation and activation. *Cell* **93**, 165–176 (1998).

973 41. Anderson, D. M. *et al.* A homologue of the TNF receptor and its ligand enhance T-cell
974 growth and dendritic-cell function. *Nature* **390**, 175–179 (1997).

975 42. Wong, B. R. *et al.* The TRAF family of signal transducers mediates NF-kappaB activation
976 by the TRANCE receptor. *J. Biol. Chem.* **273**, 28355–28359 (1998).

977 43. Wu, J., Glimcher, L. H. & Aliprantis, A. O. HCO3-/Cl- anion exchanger SLC4A2 is required
978 for proper osteoclast differentiation and function. *Proc. Natl. Acad. Sci. U. S. A.* **105**,
979 16934–16939 (2008).

980 44. Duan, X., Yang, S., Zhang, L. & Yang, T. V-ATPases and osteoclasts: ambiguous future of
981 V-ATPases inhibitors in osteoporosis. *Theranostics* **8**, 5379–5399 (2018).

982 45. Lattin, J. E. *et al.* Expression analysis of G Protein-Coupled Receptors in mouse
983 macrophages. *Immunome Res.* **4**, 5 (2008).

984 46. Bennetts, J. S. *et al.* Evolutionary conservation and murine embryonic expression of the
985 gene encoding the SERTA domain-containing protein CDCA4 (HEPP). *Gene* **374**, 153–165
986 (2006).

987 47. Zhan, Y. *et al.* Mechanism of the effect of glycosyltransferase GLT8D2 on fatty liver. *Lipids
988 Health Dis.* **14**, 43 (2015).

989 48. Movérare-Skrtic, S. *et al.* Osteoblast-derived WNT16 represses osteoclastogenesis and

990 prevents cortical bone fragility fractures. *Nat. Med.* **20**, 1279–1288 (2014).

991 49. Takeshita, S., Kikuno, R., Tezuka, K. & Amann, E. Osteoblast-specific factor 2: cloning of a
992 putative bone adhesion protein with homology with the insect protein fasciclin I. *Biochem. J*
993 **294 (Pt 1)**, 271–278 (1993).

994 50. Horiuchi, K. *et al.* Identification and characterization of a novel protein, periostin, with
995 restricted expression to periosteum and periodontal ligament and increased expression by
996 transforming growth factor beta. *J. Bone Miner. Res.* **14**, 1239–1249 (1999).

997 51. Izu, Y., Ezura, Y., Koch, M., Birk, D. E. & Noda, M. Collagens VI and XII form complexes
998 mediating osteoblast interactions during osteogenesis. *Cell Tissue Res.* **364**, 623–635
999 (2016).

1000 52. Amiri, N. & Christians, J. K. PAPP-A2 expression by osteoblasts is required for normal
1001 postnatal growth in mice. *Growth Horm. IGF Res.* **25**, 274–280 (2015).

1002 53. Wilm, B., Dahl, E., Peters, H., Balling, R. & Imai, K. Targeted disruption of Pax1 defines its
1003 null phenotype and proves haploinsufficiency. *Proc. Natl. Acad. Sci. U. S. A.* **95**, 8692–
1004 8697 (1998).

1005 54. Kimura, H., Akiyama, H., Nakamura, T. & de Crombrugghe, B. Tenascin-W inhibits
1006 proliferation and differentiation of preosteoblasts during endochondral bone formation.
1007 *Biochem. Biophys. Res. Commun.* **356**, 935–941 (2007).

1008 55. Koscielny, G. *et al.* The International Mouse Phenotyping Consortium Web Portal, a unified
1009 point of access for knockout mice and related phenotyping data. *Nucleic Acids Res.* **42**,
1010 D802-9 (2014).

1011 56. Yalcin, B., Flint, J. & Mott, R. Using Progenitor Strain Information to Identify Quantitative
1012 Trait Nucleotides in Outbred Mice. *Genetics* vol. 171 673–681 (2005).

1013 57. Ilani, T. *et al.* A secreted disulfide catalyst controls extracellular matrix composition and
1014 function. *Science* **341**, 74–76 (2013).

1015 58. Huybrechts, Y., Mortier, G., Boudin, E. & Van Hul, W. WNT Signaling and Bone: Lessons

From Skeletal Dysplasias and Disorders. *Front. Endocrinol.* **11**, 165 (2020).

59. Teufel, S. & Hartmann, C. Wnt-signaling in skeletal development. *Curr. Top. Dev. Biol.* **133**, 235–279 (2019).
60. Tong, W. *et al.* Wnt16 attenuates osteoarthritis progression through a PCP/JNK-mTORC1-PTHrP cascade. *Ann. Rheum. Dis.* **78**, 551–561 (2019).
61. Bonnet, N., Garnero, P. & Ferrari, S. Periostin action in bone. *Mol. Cell. Endocrinol.* **432**, 75–82 (2016).
62. Rajpal, G. & Arvan, P. Chapter 236 - Disulfide Bond Formation. in *Handbook of Biologically Active Peptides (Second Edition)* (ed. Kastin, A. J.) 1721–1729 (Academic Press, 2013).
63. Bulleid, N. J. & Ellgaard, L. Multiple ways to make disulfides. *Trends in Biochemical Sciences* vol. 36 485–492 (2011).
64. Feldman, T. *et al.* Inhibition of fibroblast secreted QSOX1 perturbs extracellular matrix in the tumor microenvironment and decreases tumor growth and metastasis in murine cancer models. *Oncotarget* **11**, 386–398 (2020).
65. Hanavan, P. D. *et al.* Ebselen inhibits QSOX1 enzymatic activity and suppresses invasion of pancreatic and renal cancer cell lines. *Oncotarget* **6**, 18418–18428 (2015).
66. Bouxsein, M. L. *et al.* Guidelines for assessment of bone microstructure in rodents using micro--computed tomography. *J. Bone Miner. Res.* **25**, 1468–1486 (2010).
67. Andrews, S. & Others. FastQC: a quality control tool for high throughput sequence data. (2010).
68. Kim, D., Paggi, J. M., Park, C., Bennett, C. & Salzberg, S. L. Graph-based genome alignment and genotyping with HISAT2 and HISAT-genotype. *Nat. Biotechnol.* **37**, 907–915 (2019).
69. Pertea, M. *et al.* StringTie enables improved reconstruction of a transcriptome from RNA-seq reads. *Nat. Biotechnol.* **33**, 290–295 (2015).
70. Team, R. C. & Others. R: A language and environment for statistical computing. (2013).

1042 71. Broman, K. W. *et al.* R/qtl2: Software for Mapping Quantitative Trait Loci with High-
1043 Dimensional Data and Multiparent Populations. *Genetics* **211**, 495–502 (2019).
1044 72. Morgan, A. P. argyle: An R Package for Analysis of Illumina Genotyping Arrays. *G3* **6**,
1045 281–286 (2015).
1046 73. Broman, K. W., Gatti, D. M., Svenson, K. L., Sen, Ś. & Churchill, G. A. Cleaning Genotype
1047 Data from Diversity Outbred Mice. *G3* **9**, 1571–1579 (2019).
1048 74. Love, M. I., Huber, W. & Anders, S. Moderated estimation of fold change and dispersion for
1049 RNA-seq data with DESeq2. *Genome Biol.* **15**, 550 (2014).
1050 75. Leek, J. T., Johnson, W. E., Parker, H. S., Jaffe, A. E. & Storey, J. D. The sva package for
1051 removing batch effects and other unwanted variation in high-throughput experiments.
1052 *Bioinformatics* **28**, 882–883 (2012).
1053 76. Langfelder, P. & Horvath, S. WGCNA: an R package for weighted correlation network
1054 analysis. *BMC Bioinformatics* **9**, 559 (2008).
1055 77. Langfelder, P. & Horvath, S. Fast R Functions for Robust Correlations and Hierarchical
1056 Clustering. *J. Stat. Softw.* **46**, (2012).
1057 78. Scutari, M. Learning Bayesian Networks with thebnlearnRPackage. *Journal of Statistical*
1058 *Software* vol. 35 (2010).
1059 79. Ashburner, M. *et al.* Gene Ontology: tool for the unification of biology. *Nature Genetics* vol.
1060 25 25–29 (2000).
1061 80. Blake, J. A. *et al.* The Mouse Genome Database (MGD): premier model organism resource
1062 for mammalian genomics and genetics. *Nucleic Acids Res.* **39**, D842-8 (2011).
1063 81. Carbon, S. *et al.* AmiGO: online access to ontology and annotation data. *Bioinformatics* **25**,
1064 288–289 (2009).
1065 82. Csardi, G., Nepusz, T. & Others. The igraph software package for complex network
1066 research. *InterJournal, complex systems* **1695**, 1–9 (2006).
1067 83. Giambartolomei, C. *et al.* Bayesian Test for Colocalisation between Pairs of Genetic

Association Studies Using Summary Statistics. *PLoS Genetics* vol. 10 e1004383 (2014).

84. Alexa, A. Rahnenfuhrer J. topGO: enrichment analysis for Gene Ontology. 2010. *R package version* **2**, 45 (2017).

85. Dickinson, M. E. *et al.* High-throughput discovery of novel developmental phenotypes. *Nature* **537**, 508–514 (2016).

86. Kurbatova, N., Karp, N., Mason, J. & Haselimashhadi, H. PhenStat: statistical analysis of phenotypic data. *R package version* **2**, (2015).

87. West, B. T., Welch, K. B. & Galecki, A. T. *Linear Mixed Models: A Practical Guide Using Statistical Software, Second Edition*. (CRC Press, 2014).

88. Yang, J. *et al.* FTO genotype is associated with phenotypic variability of body mass index. *Nature* **490**, 267–272 (2012).

89. Stegle, O., Parts, L., Piipari, M., Winn, J. & Durbin, R. Using probabilistic estimation of expression residuals (PEER) to obtain increased power and interpretability of gene expression analyses. *Nat. Protoc.* **7**, 500–507 (2012).

90. Hinrichs, A. S. *et al.* The UCSC Genome Browser Database: update 2006. *Nucleic Acids Res.* **34**, D590-8 (2006).

91. Lawrence, M. *et al.* Software for Computing and Annotating Genomic Ranges. *PLoS Computational Biology* vol. 9 e1003118 (2013).

92. McLaren, W. *et al.* The Ensembl Variant Effect Predictor. *Genome Biol.* **17**, 122 (2016).

93. Shorter, J. R. *et al.* Quantitative trait mapping in Diversity Outbred mice identifies two genomic regions associated with heart size. *Mamm. Genome* **29**, 80–89 (2018).

94. Mesner, L. D. *et al.* Mouse genome-wide association and systems genetics identifies Lhfp as a regulator of bone mass. *PLoS Genet.* **15**, e1008123 (2019).

95. Russell, L. emmeans: Estimated Marginal Means, aka Least-Squares Means. R package version 1.4. (2019).

96. Israel, B. A., Jiang, L., Gannon, S. A. & Thorpe, C. Disulfide bond generation in mammalian

blood serum: detection and purification of quiescin-sulfhydryl oxidase. *Free Radic. Biol. Med.* **69**, 129–135 (2014).

97. Hanna, H., Mir, L. M. & Andre, F. M. In vitro osteoblastic differentiation of mesenchymal stem cells generates cell layers with distinct properties. *Stem Cell Res. Ther.* **9**, 203 (2018).

98. Dobin, A. *et al.* STAR: ultrafast universal RNA-seq aligner. *Bioinformatics* **29**, 15–21 (2013).

99. Butler, A., Hoffman, P., Smibert, P., Papalexi, E. & Satija, R. Integrating single-cell transcriptomic data across different conditions, technologies, and species. *Nat. Biotechnol.* **36**, 411–420 (2018).

100. Stuart, T. *et al.* Comprehensive Integration of Single-Cell Data. *Cell* **177**, 1888-1902.e21 (2019).

101. Tirosh, I. *et al.* Dissecting the multicellular ecosystem of metastatic melanoma by single-cell RNA-seq. *Science* **352**, 189–196 (2016).

Supplemental Figure 1. Characterization of the experimental cohort. a) Allele frequency per chromosome, across the DO mouse cohort. b) Heritability for each trait. c) Bone volume fraction and max load across the DO cohort. Insets are micro-CT images representing low and high bone volume fraction.

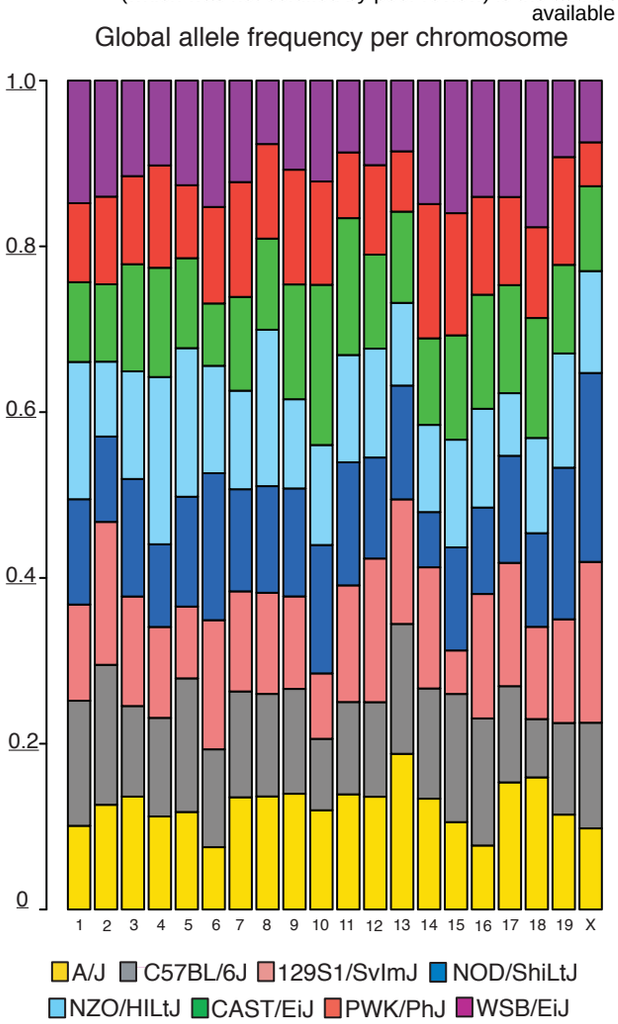

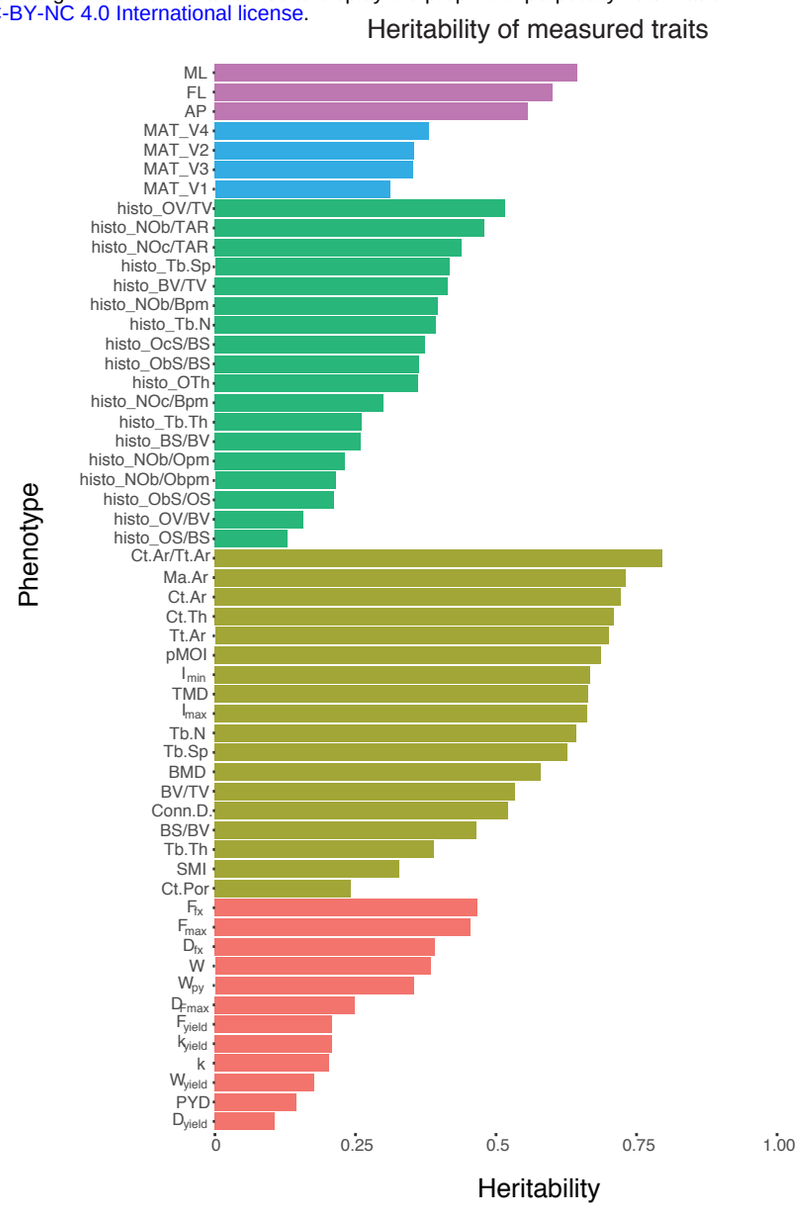

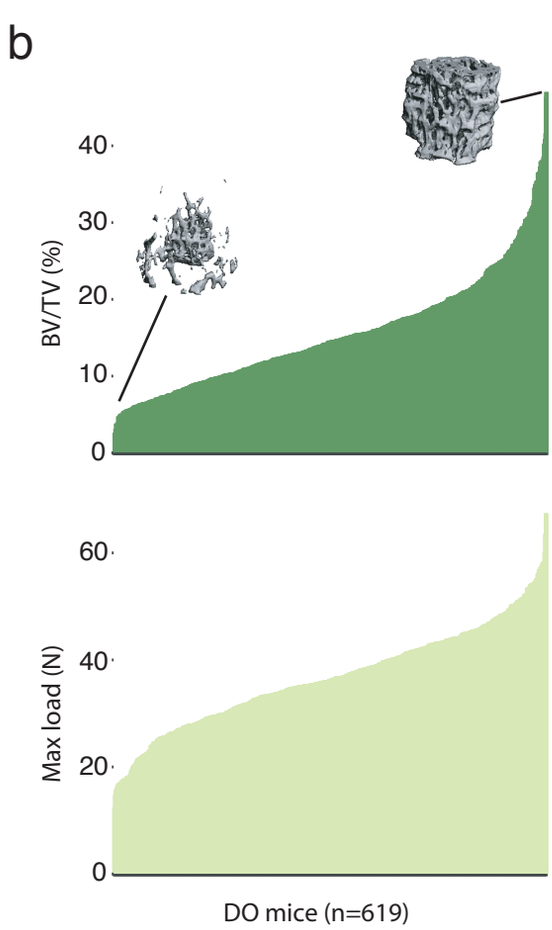

Supplemental Figure 2. Significant QTL associations.
Twenty-eight mapped QTL exceeding permutation-based LOD score thresholds (alpha=0.05)

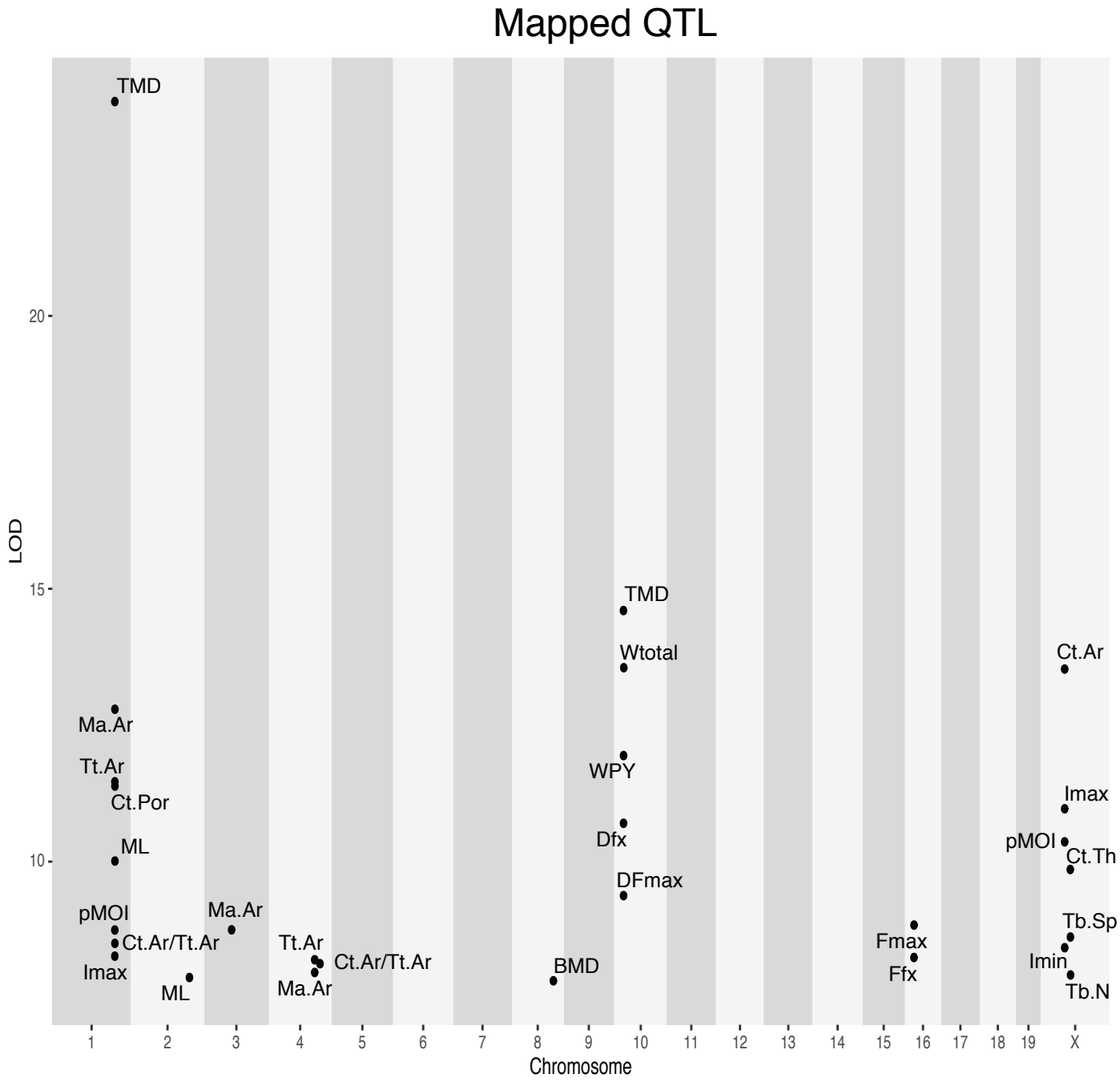

Supplemental Figure 3. Overlap between BMD GWAS SNPs and QTL loci. Each panel corresponds to a QTL locus's syntenic human region. Red circles represent BMD GWAS SNPs in the locus. The horizontal lines represent the genome-wide significance threshold (P = 5x10-8). Not all genes are shown.

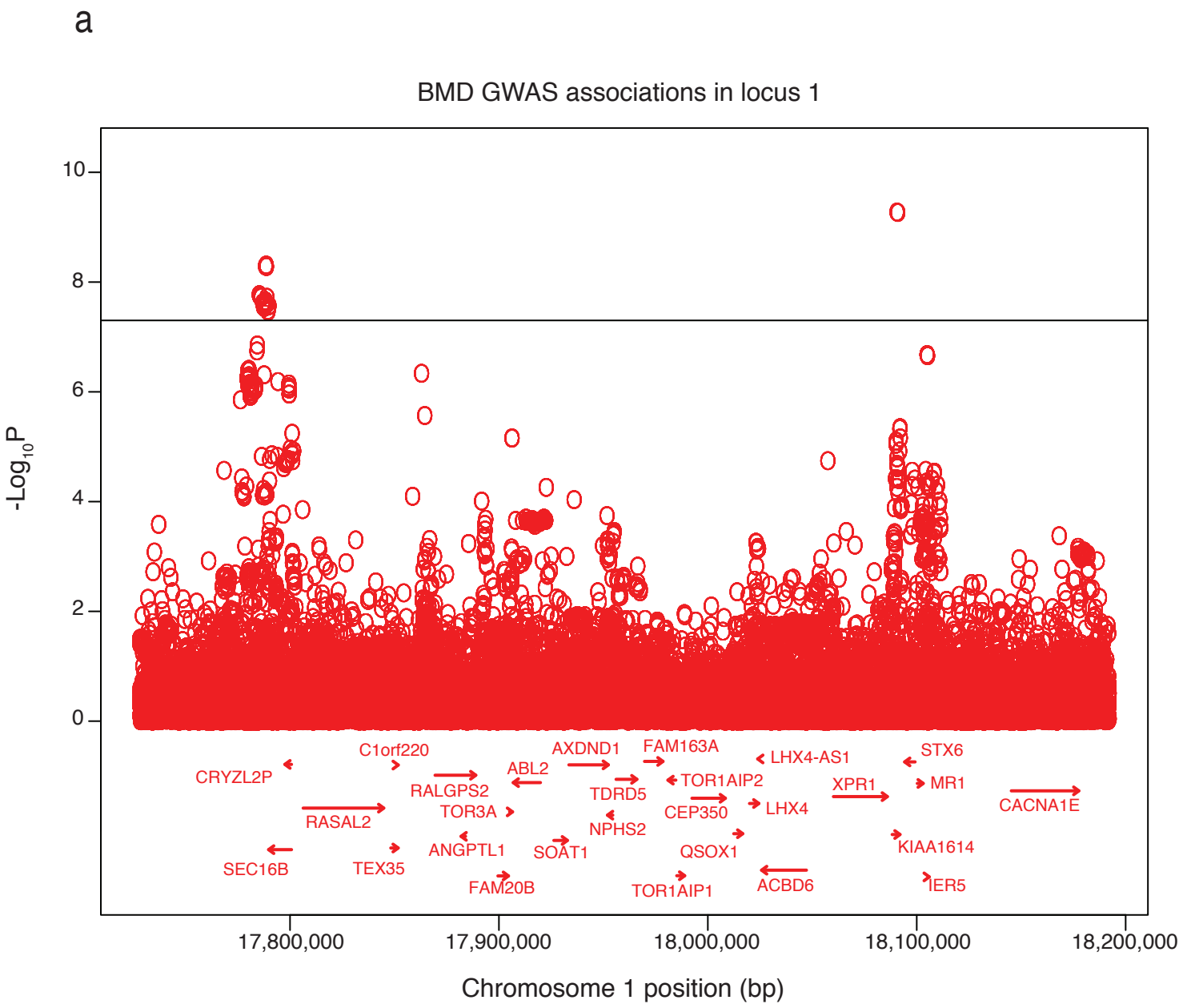

b

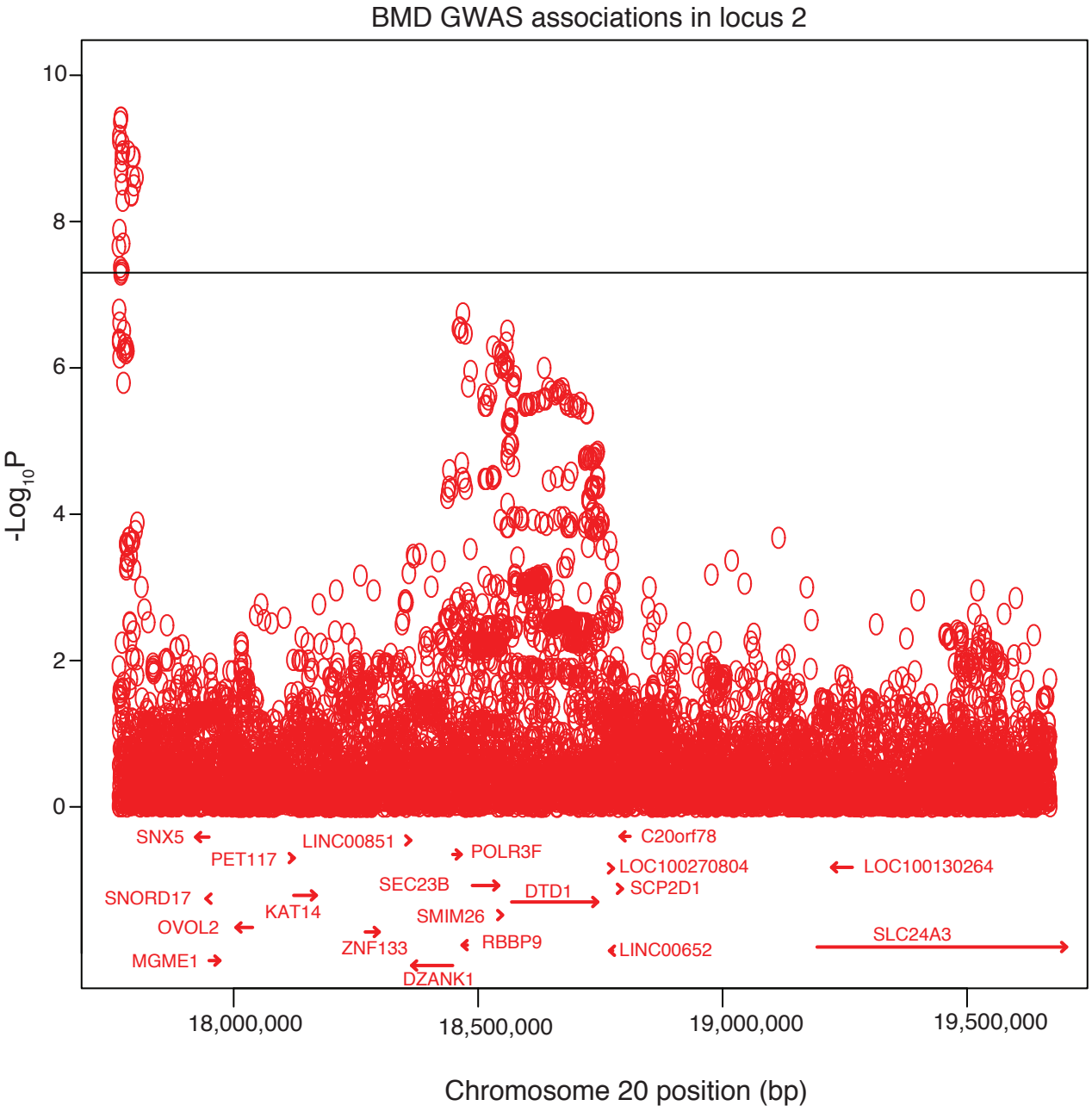

C

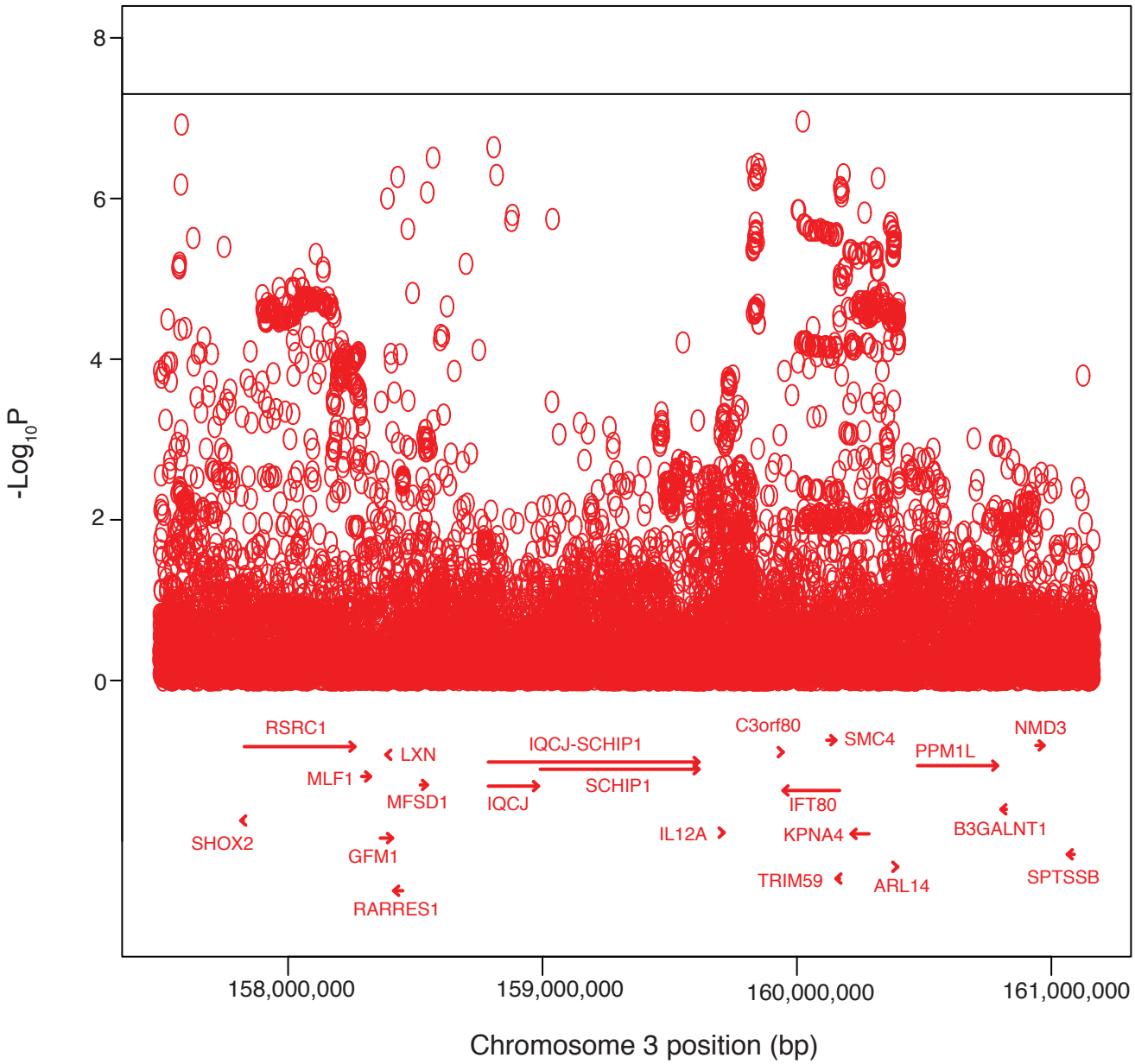

d

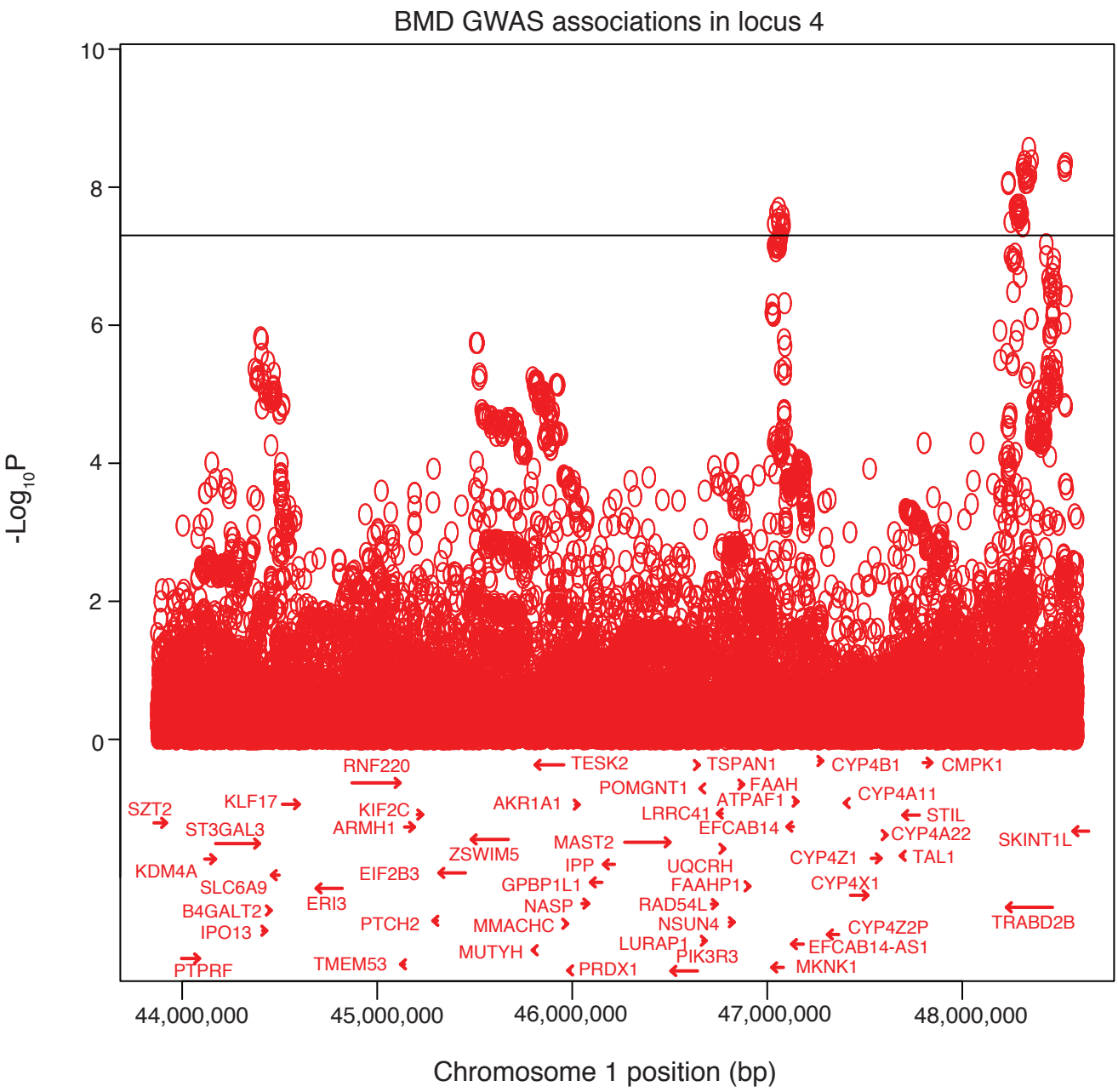

e

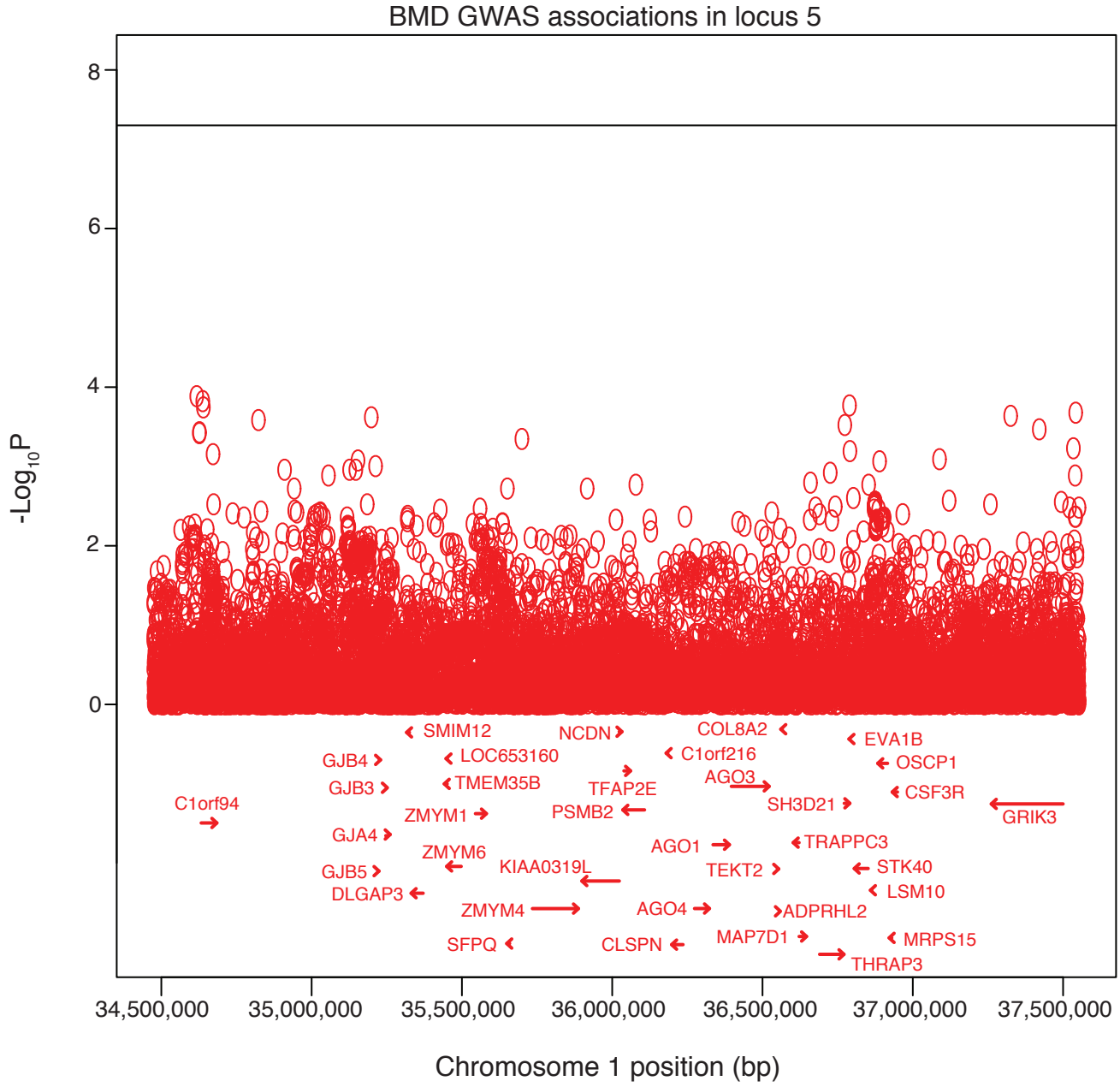

f

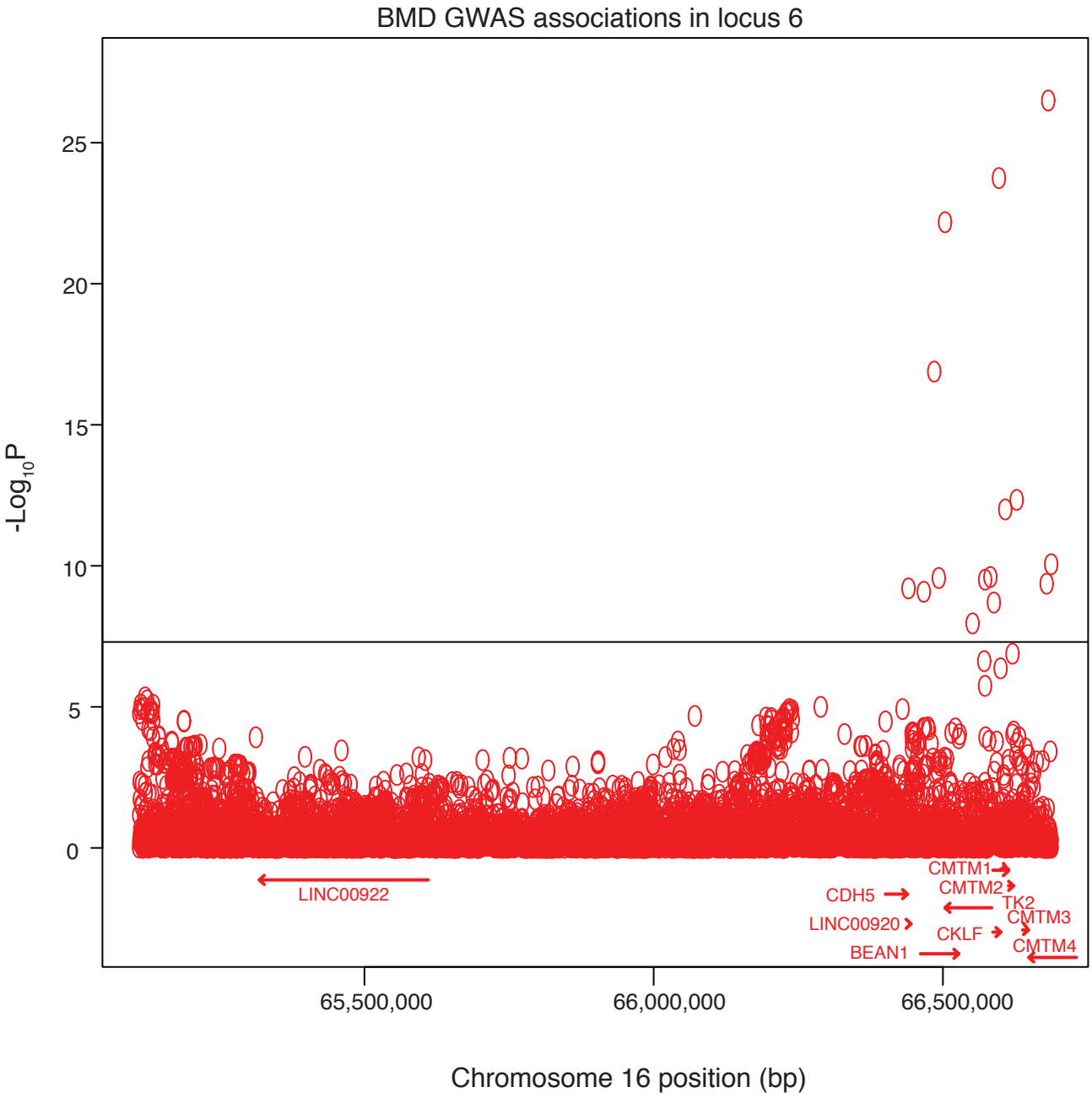

g

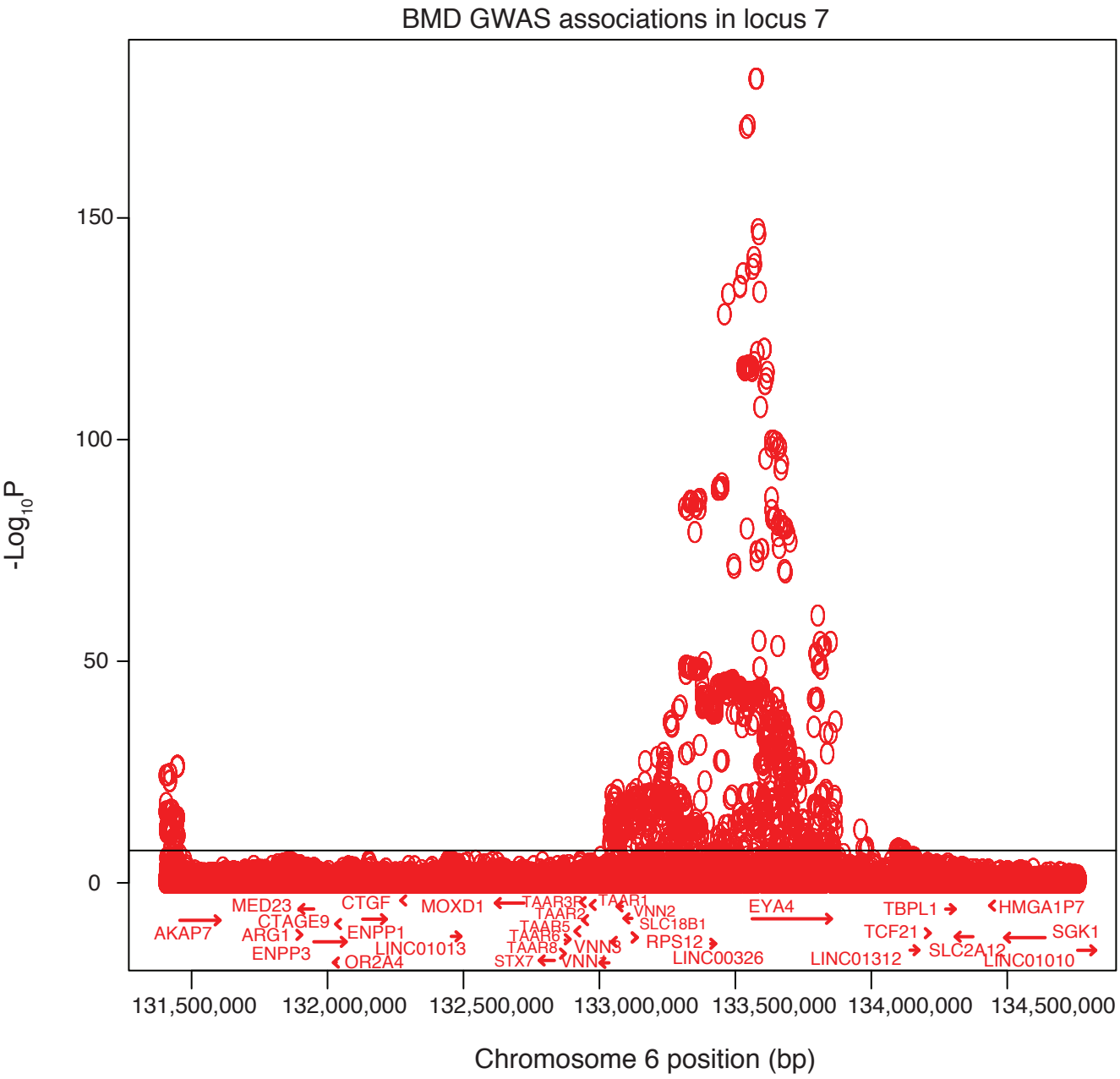

h

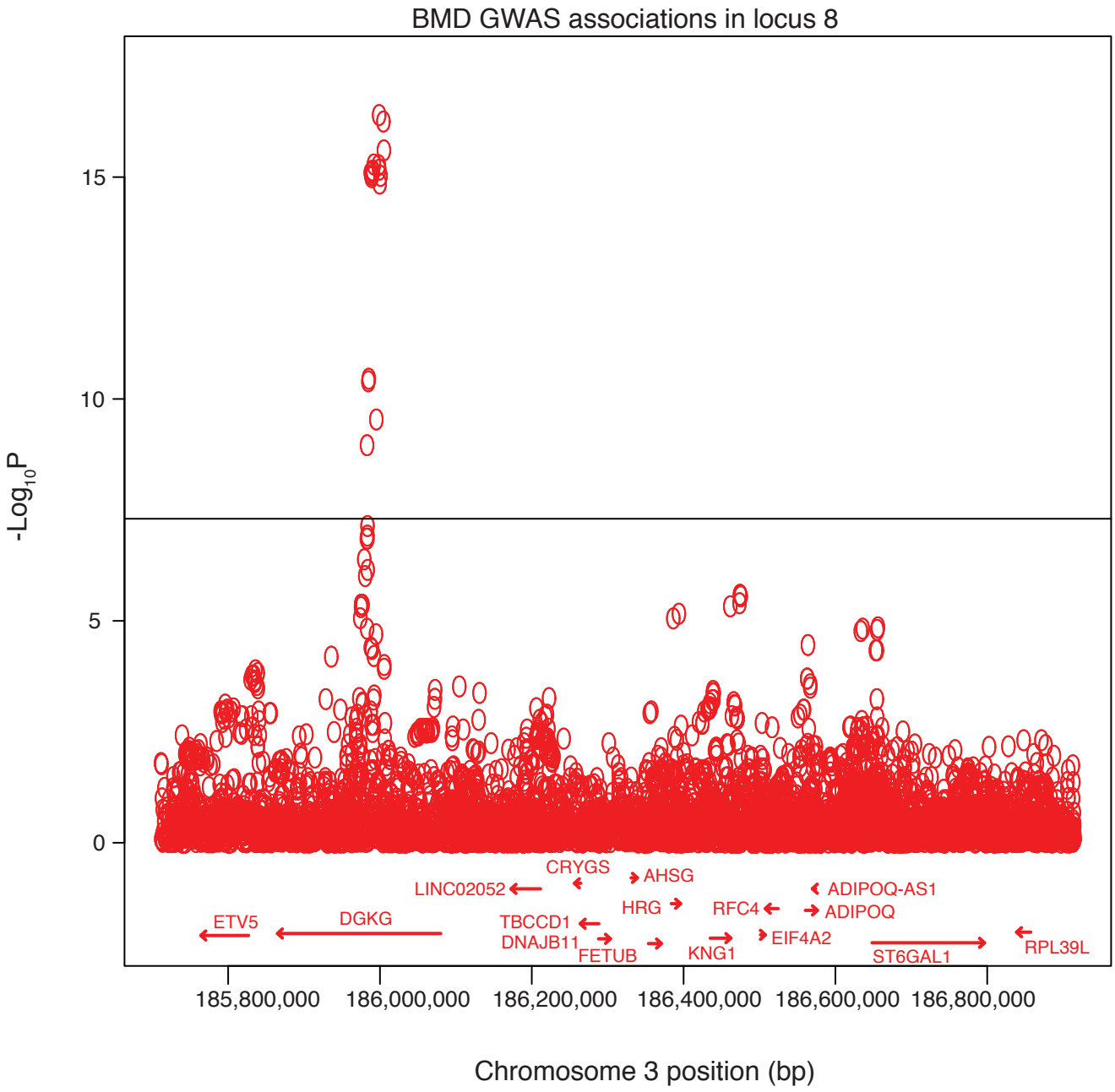

i

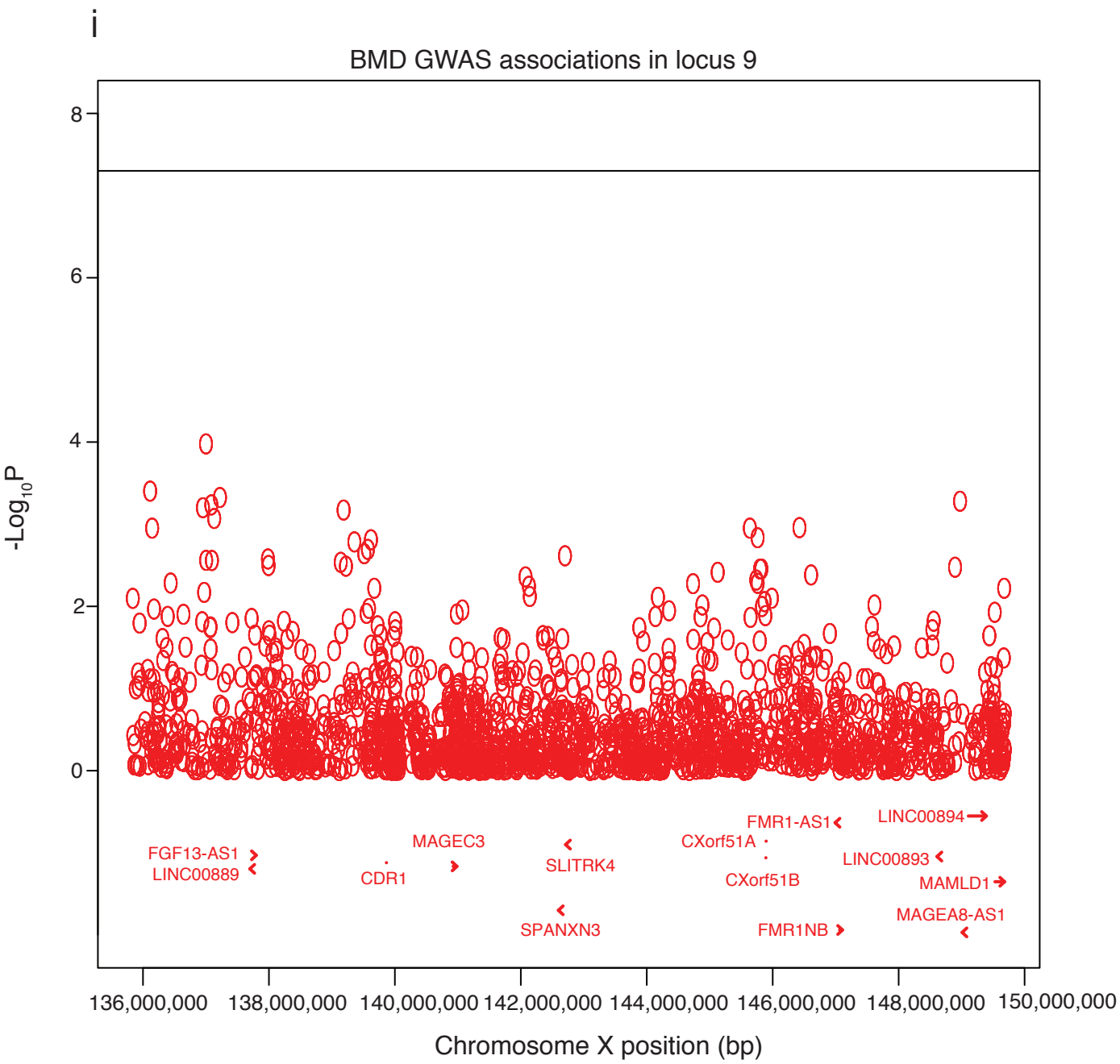

j

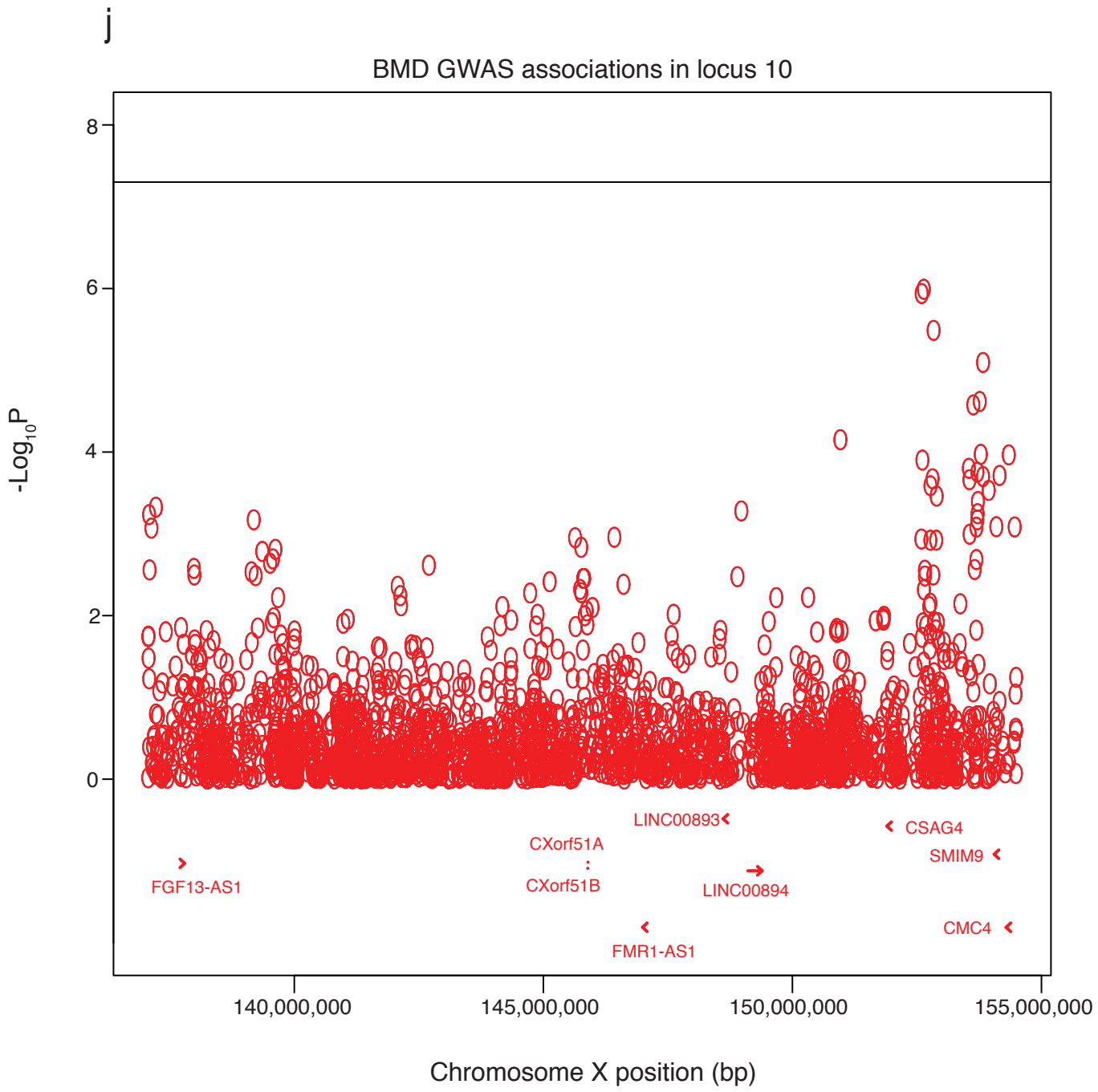

Supplemental figure 4. ML mapping in a replication cohort. The top panel shows allele effects for the DO founders for ML in an interval on chromosome 1 (Mbp). Y-axis units are best linear unbiased predictors (BLUPs). The bottom panel shows the QTL scan.